Near-surface oceanic kinetic energy distributions from drifter observations and numerical models

Brian K. Arbic[1,*], Shane Elipot[2,*], Jonathan M. Brasch[3], Dimitris Menemenlis[4], Aurélien L. Ponte[5], Jay F. Shriver[6], Xiaolong Yu[5,+], Edward D. Zaron[7], Matthew H. Alford[8], Maarten C. Buijsman[9], Ryan Abernathey[10], Daniel Garcia[3], Lingxiao Guan[3], Paige E. Martin[10,11], Arin D. Nelson[1,12]

***These authors contributed equally to this study.**
+Now at: School of Marine Sciences, Sun Yat-sen University, Zhuhai, China

[1]Department of Earth and Environmental Sciences, University of Michigan, Ann Arbor, MI, USA
[2]Rosenstiel School of Marine and Atmospheric Science, University of Miami, Miami, FL, USA
[3]Department of Electrical Engineering and Computer Science, University of Michigan, Ann Arbor, MI, USA
[4]Jet Propulsion Laboratory, California Institute of Technology, Pasadena, CA, USA
[5]Ifremer, Université de Brest, CNRS, IRD, Laboratoire d'Océanographie Physique et Spatiale, IUEM, Brest, France
[6]Naval Research Laboratory, Stennis Space Center, Mississippi,USA
[7]College of Earth, Ocean, and Atmospheric Sciences, Oregon State University, Corvallis, OR, USA
[8]Scripps Institution of Oceanography, University of California San Diego, La Jolla, California, USA
[9]School of Ocean Science and Engineering, University of Southern Mississippi, Stennis Space Center, Mississippi
[10]Lamont-Doherty Earth Observatory, Columbia University, New York City, NY, USA
[11]Department of Physics, University of Michigan, Ann Arbor, MI, USA
[12]Graduate School of Oceanography, University of Rhode Island, Kingston, RI, USA

Key Points:

- We examine frequency content of ocean kinetic energy (KE) at the sea surface (0 m) and 15 m depth with global drifter data and two models.
- Near-surface near-inertial and tidal kinetic energy in numerical models are sensitive to atmospheric forcing frequency and damping.
- The ratio of 0m KE to 0m+15m KE in models and observations lie within error bars of each other over some latitudes and frequency bands.

Corresponding author: Brian K. Arbic & Shane Elipot, `arbic@umich.edu` & `selipot@miami.edu`

Abstract

The geographical variability, frequency content, and vertical structure of near-surface oceanic kinetic energy (KE) are important for air-sea interaction, marine ecosystems, operational oceanography, pollutant tracking, and interpreting remotely sensed velocity measurements. Here, KE in high-resolution global simulations (HYbrid Coordinate Ocean Model; HYCOM, and Massachusetts Institute of Technology general circulation model; MITgcm), at the sea surface (0 m) and 15 m, are respectively compared with KE from undrogued and drogued surface drifters. Global maps and zonal averages are computed for low-frequency (< 0.5 cpd), near-inertial, diurnal, and semi-diurnal bands. Both models exhibit low-frequency equatorial KE that is low relative to drifter values. HYCOM near-inertial KE is higher than in MITgcm, and closer to drifter values, probably due to more frequently updated atmospheric forcing. HYCOM semi-diurnal KE is lower than in MITgcm, and closer to drifter values, likely due to inclusion of a parameterized topographic internal wave drag. A concurrent tidal harmonic analysis in the diurnal band demonstrates that much of the diurnal flow is non-tidal. We compute a simple proxy of near-surface vertical structure, the ratio of 0 m KE to 0 m KE plus 15 m KE in model outputs, and undrogued KE to undrogued KE plus drogued KE in drifter observations. Over most latitudes and frequency bands, model ratios track the drifter ratios to within error bars. Values of this ratio demonstrate significant vertical structure in all frequency bands except the semidiurnal band. Latitudinal dependence in the ratio is greatest in diurnal and low-frequency bands.

Plain Language Summary

It is important to map and understand ocean surface currents because they affect climate and marine ecosystems. Recent advances in global ocean models include the addition of astronomical tidal forcing alongside atmospheric forcing, and the usage of more powerful computers that can resolve finer features. Here we evaluate ocean surface currents in high-resolution simulations of two different ocean models through comparison with observations from surface drifting buoys. We examine near-inertial motions, forced by fast-changing winds, semidiurnal tides, forced by the astronomical tidal potential, diurnal motions, arising from tidal and other sources, and low-frequency currents and eddies, forced by atmospheric fields. Global patterns in the models and drifters are broadly consistent. The two models differ in their degree of proximity to drifter measurements in the near-inertial band, most likely due to different update intervals for atmospheric forcing, and in the semidiurnal band, most likely due to different damping schemes. A simple proxy for vertical structure of the currents, measured by differences in drifter flows at the surface vs. 15 meters depth, is tracked reasonably well by the models. Discrepancies between models and observations motivate future improvements in the models.

1 Introduction

This paper presents a comprehensive comparison of the geographical distribution and frequency content of near-surface kinetic energy (KE) from two different global high resolution models with observations from NOAA's Global Drifter Program (GDP). We divide KE into different frequency bands of interest via spectral analysis. We compare model results at the sea surface with results from undrogued drifters, and model results from 15 m depth with results from drogued drifters. Our ability to examine a wide range of frequencies is enabled by the employment of astronomical tidal forcing alongside atmospheric forcing in both models. We compute a proxy ratio of vertical structure, the ratio of KE at the surface divided by the sum of surface KE and 15 m KE, and compare this ratio in the models vs drifters. The proxy ratio that we use is an incomplete measure of vertical structure. It is emphasized here because it can be computed on a global-scale from drifter observations, thus offering a novel global-scale examination of the abil-

ity of models to simulate aspects of vertical KE structure in the upper ocean. In the near future, the global near-surface ocean velocity field may be measured by remote sensing missions, such as the potential "Odysea" mission. Until such missions are launched, models such as those used here, and drifter observations, will be the best way to map the global ocean surface velocity field over a wide range of frequency bands. Even after such missions are launched, drifter observations will serve as an important "ground truth" dataset, and models will continue to be important interpretive tools. This manuscript aims at taking a wide-ranging, holistic descriptive approach. There are many sources of difference between the two models used, and between the models and drifter data. In addition, there are many important sensitivities and processes that remain to be explored, far more than can be examined in one paper. We will note the multiple sources of difference and unexplored sensitivities and processes as they arise throughout the manuscript. A major aim of this manuscript is to motivate future studies on particular aspects of the model-observation and model-model discrepancies that we document here. We believe that a paper focused on a broad-brush analysis is well-suited for highlighting potential areas for process studies and model improvements.

Oceanic surface currents are relevant for a range of multi-disciplinary scientific topics and operational applications (Elipot & Wenegrat, 2021). For instance, surface currents are major actors in two crucial components of the climate system, the air-sea transition zone (Cronin & Coauthors, 2019) and marine ecosystems (Lévy et al., 2018). Maps of surface currents are useful for understanding ocean dynamics, assessing operational ocean modeling, enabling search-and-rescue missions, and tracking oil spills, plastics, and other marine pollutants. Many of these applications, including predicting Lagrangian trajectories of water parcels in the near-surface ocean, understanding air-sea transfer, and others, require knowledge not only of currents but also their vertical structure near the oceanic surface (Beron-Vera et al., 2019).

Despite the importance of near-surface currents, not enough is known about their space-time variability. Mapping near-surface oceanic currents on a global scale is a formidable task. Quantifying high-frequency motions such as near-inertial flows (e.g., Pollard & Millard, 1970; Alford, 2003a, 2003b; Furuichi et al., 2008; Chaigneau et al., 2008; Simmons & Alford, 2012), semidiurnal tides, diurnal tides and other diurnal motions, and the internal gravity wave continuum (Garrett & Munk, 1975) requires high-frequency sampling (e.g., at approximately hourly intervals). Time series from moored current meters can be used to separate high-frequency motions from lower-frequency motions including Ekman flows, mesoscale eddies, and the oceanic general circulation. Another advantage of mooring lines is the delivery of observations below the ocean surface. However, moored data are expensive to deploy and are available only at a relatively small number of geographical locations (see, for instance, Figure 1 of Luecke et al., 2020). Global-scale surface currents can be computed from satellite altimeter measurements of sea-surface height (SSH), providing that tides are removed and the geostrophic assumption is applied to the tide-corrected SSH fields. However, altimetry cannot detect near-inertial or Ekman flows, due to the negligible SSH signal in these motions. Altimetry measurements are also infrequent in time. The repeat time of the TOPEX/Jason series, for instance, is about 10 days. The geostrophic velocities computed from altimetry leave out high-frequency contributions to the velocity and hence KE fields.

The drifting buoys, or drifters, of the GDP (Lumpkin et al., 2017) yield a global dataset of near-surface ocean velocity in situ estimates. Drifters have been used in many previous studies of low-frequency oceanic flows, including the mean dynamic topography (Maximenko et al., 2009), Ekman flows (Elipot & Gille, 2009), and the eddying general circulation (Thoppil et al., 2011). Recently, drifters have also been used to quantify high-frequency motions such as tides (Poulain & Centurioni, 2015; Kodaira et al., 2015; Zaron & Elipot, 2021). Elipot et al. (2016) derived an hourly drifter product and demonstrated that it resolves motions at a wide range of frequencies.

Model-drifter comparison over a wide range of frequency bands is now possible, due to the emergence of a new class of high-resolution global ocean models that simultaneously include astronomical tidal forcing and atmospheric forcing (e.g., Arbic et al., 2010, 2012, 2018; Arbic, 2022; Buijsman et al., 2020; Müller et al., 2012; Waterhouse et al., 2014; Rocha, Chereskin, et al., 2016; Rocha, Gille, et al., 2016). In these models, internal tides and mesoscale eddies co-exist and interact (Shriver et al., 2014; Buijsman et al., 2017; Nelson et al., 2019). As shown first in Müller et al. (2015) and later in other studies (e.g., Rocha, Chereskin, et al., 2016; Savage et al., 2017a, 2017b; Qiu et al., 2018; Torres et al., 2018; Luecke et al., 2020), such models are beginning to partially resolve the internal gravity wave (IGW) continuum (Garrett-Munk spectrum; Garrett & Munk, 1975). Yu et al. (2019) compared KE, over various low- and high-frequency bands, from the hourly drifter dataset and output from a high-resolution Massachusetts Institute of Technology general circulation model (MITgcm; Marshall et al., 1997) simulation, forced by both the astronomical tidal potential and atmospheric fields. The MITgcm simulation employed in Yu et al. (2019), designated as LLC4320, is further used here in a three-way comparison with drifter observations and a global internal tide and gravity wave simulation of the HYbrid Coordinate Ocean Model (HYCOM; Chassignet et al., 2009), the backbone operational model of the United States Navy.

Global IGW model simulations, especially MITgcm LLC4320 and from HYCOM, have been widely used by the community, to plan for field campaigns (e.g., J. Wang et al., 2018), understand interactions between motions at different length and time scales (e.g., Pan et al., 2020), and provide boundary forcing for higher-resolution regional models (Nelson et al., 2020). HYCOM and MITgcm LLC4320 have been used to quantify the relative contributions of low- and high-frequency motions to SSH and KE as a function of geographical location (e.g., Richman et al., 2012; Savage et al., 2017a, 2017b; Rocha, Chereskin, et al., 2016; Rocha, Gille, et al., 2016; Qiu et al., 2018; Torres et al., 2018). The energetics of different classes of oceanic motions are of interest in their own right (Ferrari & Wunsch, 2009). Global IGW models offer the potential for examining energy exchanges between different classes of oceanic motions, as has been seen in observations (Le Boyer & Alford, 2021). Quantitative mapping of low- and high-frequency motions is important for satellite missions including the Surface Water Ocean Topography (SWOT) mission (Morrow et al., 2019), planned for launch in 2022, which will measure SSH at high resolution in two-dimensional swaths. Remote sensing missions focused on measuring near-surface ocean velocities, such as the existing airborne Sub-Mesoscale Ocean Dynamics Experiment (S-MODE) mission (Rodriguez et al., 2020), and proposed velocity-measuring satellite missions (Ardhuin et al., 2019; Rodriguez et al., 2020), now under the umbrella name "Odysea", will benefit from quantification of high- and low-frequency KE as well. Because HYCOM and MITgcm LLC4320 are widely used, it is important to compare these models to observations. A summary of model comparisons of HYCOM and MITgcm LLC4320 tidal simulations with mooring and altimeter observations is provided in Arbic et al. (2018) and Arbic (2022). MITgcm LLC4320 has also been compared to along-track Acoustic Doppler Current Profiler (ADCP) data (Rocha, Chereskin, et al., 2016; Chereskin et al., 2019).

As demonstrated by Yu et al. (2019), drifters are an excellent dataset for revealing strengths and weaknesses of numerical ocean simulations. For instance, Yu et al. (2019) showed that LLC4320 semidiurnal tidal KE was too strong, and near-inertial KE too weak, relative to drifter observations. Here, we build upon their study through intercomparison of HYCOM, MITgcm LLC4320, and drifters. We employ an udpated analysis of the drifters, that yields fewer spatial gaps than the analysis employed in Yu et al. (2019), especially near the equator. The HYCOM and MITgcm LLC4320 simulations differ in several respects, and we anticipate that they will perform differently in comparisons to drifters. We especially anticipate differences in the near-inertial bands, due to more frequent updates of the wind fields in HYCOM (3 hours) relative to MITgcm LLC4320 (6 hours), and in the semidiurnal tidal band, due to the lack of a parameterized topographic

wave drag in MITgcm LLC4320. In HYCOM simulations, a parameterized topographic internal wave drag is included in order to roughly account for the damping of tidal motions due to breaking small-scale internal tides that are unresolved in global models (Arbic et al., 2010, 2018; Ansong et al., 2015; Buijsman et al., 2016, 2020; Arbic, 2022). Ansong et al. (2015) demonstrated that the SSH signature of internal tides in HYCOM is closer to altimetry observations when the HYCOM simulations contain a wave drag than when they do not. Here we examine the impact of including wave drag (as in HYCOM) vs. excluding it (as in LLC4320) on near-surface semidiurnal KE. The diurnal band is also of special interest. Here, we complement the frequency spectral analysis of the diurnal band in the models with a tidal harmonic analysis. Differences between maps computed from frequency spectra versus tidal harmonic analysis can reveal whether the diurnal band also has significant non-tidal sources in the models.

An examination of the vertical structure of near-surface currents will aid our understanding of the air-sea exchange of heat, momentum, and gases, and of the dispersal of pollutants and biologically important tracers (Elipot & Wenegrat, 2021). The vertical structure of velocity has important implications for the ongoing S-MODE airborne mission and proposed satellite missions focusing on surface ocean velocity measurements (Ardhuin et al., 2019; Rodriguez et al., 2020). Such missions will need information on the frequency dependence of vertical structure in order to interpret the implications of surface current measurements for subsurface oceanic conditions.

Here we examine a vertical structure proxy ratio, based upon the relative strengths of KE at the sea surface and at 15 m depth, the depths accessible to undrogued and drogued drifters. To our knowledge, a global comparison of the 0 and 15 m KE, for both high- and low-frequency motions, has not been done before. As in Yu et al. (2019), we use both undrogued and drogued drifters which provide estimates of oceanic velocity at 0 m (sea surface) and 15 m, respectively. Accordingly, we compare model results at 0 m to undrogued drifter results, and model results at 15 m to drogued drifter results. Error bars on the vertical structure proxy ratio in drifter observations are large, especially for near-inertial and tidal motions, and windage (erroneous slips of water past drifters) are a known problem in undrogued drifter observations (Section 2.4). Nevertheless, the model ratios, which suffer from completely different biases and errors, follow the drifter ratios over most latitudes and most frequency bands.

The paper is organized as follows. Section 2 describes the HYCOM simulation, the MITgcm LLC4320 simulation, and the drifter observations. This section also discusses the vertical momentum mixing schemes impacting modeled vertical structure in the upper ocean, and describes the data analysis methods. The main results of the paper, consisting of rotary frequency spectra and maps and zonal averages of KE over specific frequency bands, are provided in Section 3. A discussion of the results is put forth in Section 4, while Section 5 provides a summary and concluding remarks.

2 Data and Methods

We begin this section with a brief discussion of the limitations inherent in running and analyzing large global simulations. The simulations used in this study are computationally expensive and finding multiple years of output to analyze is not yet possible. Further, the individual years examined in this study are different for HYCOM and MITgcm LLC4320. The latter simulation was a "one-off", run for just over a year, and is, to the best of our knowledge, the most computationally expensive ocean numerical simulation ever undertaken. The HYCOM simulations, on the other hand, comprise the hydrodynamical backbone of US Navy ocean forecasting, and as such are constantly being improved and re-run. To find HYCOM simulations run during the same year as the MITgcm LLC4320 simulation, one would have to return to older HYCOM simulations, which have known drawbacks that have since been fixed. The centers that run these sim-

ulations do not coordinate with each other, and the many differences between the models, including but not limited to the update intervals of their respective atmospheric forcing fields, cannot be easily reconciled. Although "apples-to-apples" comparisons are not feasible, we still believe that much can be learned from comparing their outputs to observations and to each other.

2.1 HYCOM simulation

The global HYCOM simulation employs nominal 1/25° horizontal grid spacing and 41 hybrid layers (Bleck, 2002) covering the vertical direction. HYCOM employs terrain-following coordinates in shallow waters, and isopycnal coordinates in the subsurface open-ocean. In the near-surface open-ocean, the uppermost 14 layers are in z-mode, with seven z-levels, having spacing ranging from 1.00 to 6.87 m, in the uppermost 30 m (Figure 1). The HYCOM "0 m" (surface) results actually represent the mid-point of the uppermost layer. The HYCOM "15 m" results represent interpolations to 15 m. The interpolation largely reflects results from the HYCOM level at 13.185 m, which lies in between adjacent levels at 8.38 and 18.55 m. The latter three depth values represent mid-depth points of the respective vertical layers in which they lie. HYCOM employs the widely used K-Profile Parameterization (KPP) scheme (Large et al., 1994) for vertical mixing. Atmospheric forcing fields from the U.S. Navy Global Environmental Model (NAVGEM; Hogan et al., 2014) are applied every three hours and converted to surface fluxes using the bulk formulae of Kara et al. (2000). HYCOM uses relative winds (10 m wind speed minus ocean surface current speed) to compute wind stress. We use a 360-day record of hourly snapshots of surface and 15-meter horizontal velocity fields, starting on 1 January 2014, and produced with a 75 second baroclinic timestep.

HYCOM's tidal forcing includes the two largest diurnal components (K_1 and O_1) and the three largest semidiurnal components (M_2, S_2, and N_2). These five constituents capture most of the tidal variability in the oceans. Collectively, they dissipate 3.437 TW (Egbert & Ray, 2003), while the largest eight tidal constituents (the five above, plus P_1, Q_1, and K_2) dissipate 3.508 TW, only 2% larger than the dissipation rate of the five constituents included in HYCOM. The Self-attraction And Loading (SAL; Hendershott, 1972; Ray, 1998) term is taken from the altimetry-constrained TPXO8 barotropic tide model (Egbert et al., 1994; Egbert & Erofeeva, 2002). The HYCOM parameterized topographic wave drag scheme, taken from Jayne and St. Laurent (2001), is tuned to minimize the M_2 surface elevation errors with respect to TPXO8. The HYCOM simulation analyzed here employs a perturbation (Ngodock et al., 2016), generated with an Augmented State Ensemble Kalman Filter (ASEnKF), that reduces the area-weighted error of the surface tidal elevations, computed with respect to TPXO8 in waters deeper than 1000 m and latitudes equatorward of 66°, to 2.6 cm. Other than this indirect and offline use of data assimilation techniques, the HYCOM simulation is free-running (non-assimilative).

2.2 MITgcm LLC4320 simulation

LLC4320 is a global MITgcm free-running (non-assimilative) simulation with nominal 1/48° horizontal grid spacing and 90 vertical z-levels. There are 13 z-levels in the uppermost 30 m, with thickness ranging from 1.0 to 4.6 m (Figure 1). As with HYCOM, the MITgcm LLC4320 "0 m" (surface) results represent the mid-point of the uppermost level. The LLC4320 "15-m" velocities are taken from the 9th grid cell from the surface, which spans 13.26 to 16.1 m depth. LLC4320 also employs the KPP vertical mixing scheme. LLC4320 is forced by the full luni-solar astronomical tidal potential and by six-hourly atmospheric fields from the 0.14° European Centre for Medium-Range Weather Forecasting (ECMWF) operational model analysis, starting in 2011. The ECMWF atmospheric fields are converted to surface fluxes using the bulk formulae of Large and Yeager (2004) and the dynamic/thermodynamic sea ice model of Losch et al. (2010). The computation of air-sea momentum exchange is based on surface-relative wind, that is, ocean and

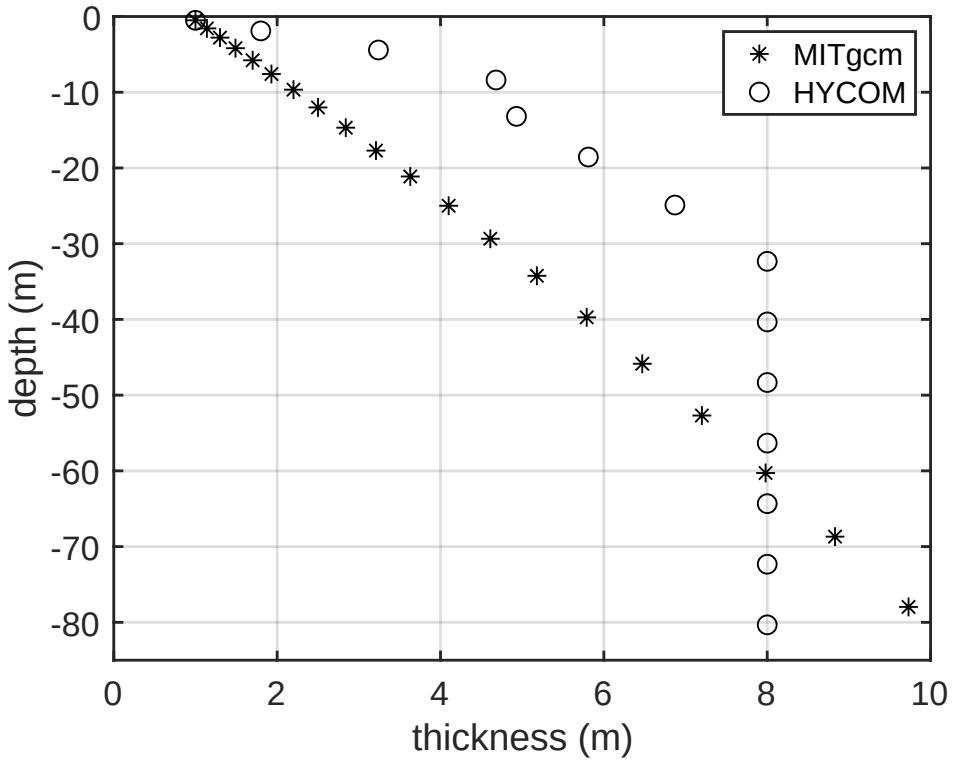

Figure 1. Near-surface vertical discretization used in the HYCOM and MITgcm LLC4320 simulations. The plot displays the grid cell thicknesses as a function of the midpoint depths of each grid cell.

sea-ice surface velocity are subtracted from 10-m atmospheric wind prior to computing surface stress. The LLC4320 integration time step is 25 s. We use a year-long record of near-surface horizontal velocity fields, saved as hourly snapshots, beginning on 12 November 2011.

We have found that the tidal forcing in the LLC4320 simulation has inadvertently been overestimated by a factor of 1.1121 while the SAL term has been omitted. The effects of these tidal forcing errors on LLC4320 tides will be reported on in detail elsewhere. In the results shown here, LLC4320 KE in semidiurnal and diurnal bands is not corrected for these errors. We note again that the LLC4320 simulation does not employ a parameterized topographic wave drag.

2.3 Vertical momentum forcing and mixing near the surface

Here we discuss the near-surface vertical momentum mixing parameterizations in the HYCOM and LLC4320 simulations. If momentum is input at the surface of the ocean, differences between KE at 0 and 15 m will depend on how momentum is mixed downward. In models the downward mixing of momentum is controlled by the vertical mixing scheme employed, in particular, the assumed vertical profile of vertical viscosity. Both the HYCOM and LLC4320 simulations employ the KPP scheme to set vertical viscosity but there are a few differences in the details of KPP implementation. In particular, the LLC4320 simulation has finer vertical discretization near the surface (13 levels in the uppermost 30 m vs 7 for HYCOM, see Figure 1); the reference buoyancy and reference velocity used to compute KPP boundary layer depth, B_r and V_r, respectively, in Equation 21 of Large et al. (1994) is computed in the surface 1-m-thick level for LLC4320 and in the top 10% of the boundary layer depth in HYCOM; and the critical Richardson number R_{ic} is 0.356 in LLC4320 while it is 0.25 in HYCOM.

Within the KPP scheme (Large et al., 1994), the vertical viscosity is a cubic profile of depth, which yields increasing viscosity values from a finite surface value to a subsurface maximum and then decreasing values below this maximum, down to a background viscosity at the base of the KPP boundary layer. When such a cubic profile, or a linear profile, is applied to the wind-driven Ekman momentum equation for the surface boundary layer, this results in a frequency-dependent shear. This shear is minimum at the inertial frequency and increases away from the inertial frequency (Elipot, 2006). This theoretical framework is useful for understanding how the locally-wind-driven component of oceanic currents (J. M. Lilly & Elipot, 2021), ranging from the inertial frequency to low-frequency Ekman motions, can be sheared in the upper 15 m of the ocean. In addition, upper-ocean stratification modulates the ultimate penetration depth of wind momentum (Large & Crawford, 1995; Crawford & Large, 1996; Elipot & Gille, 2009; Dohan & Davis, 2011; J. M. Lilly & Elipot, 2021).

Some guidance regarding the sensitivity of the KPP scheme to the various empirical parameters that it contains is available in Van Roekel et al. (2018) and Li et al. (2019). A comparison of the performance of KPP relative to other widely used vertical mixing schemes in a HYCOM simulation can be found in Pottapinjara and Joseph (2022). They showed that some schemes can be better than others at some locations and some seasons but that there is no universally "best" answer. Quantifying the exact impact of the HYCOM and LLC4320 KPP implementation details would require computationally expensive sensitivity experiments, which are beyond the scope of the present study.

2.4 Ocean Surface Drifters

In situ estimates of ocean near-surface velocities are obtained from the NOAA's GDP (Lumpkin et al., 2017) which maintains an array of surface drifting buoys, currently tracked by the Global Positioning System and previously by the Argos system. We use

version 1.04c of the hourly high-frequency dataset (Elipot et al., 2016) containing 17,324 individual surface drifter trajectories from October 1987 to June 2020, totalling ∼166M estimates of hourly positions and velocities. The spatial coverage of the drifter dataset is global, yet inhomogeneous with higher data density in convergence zones in the middle of ocean gyres, and sparse observations at the equator due to Ekman divergence, which tends to disperse drifters away (Elipot et al., 2016). The usage of more than 30 years of drifter data, in contrast to the one year of output from each of the HYCOM and MITgcm LLC4320 simulations, is another source of difference that may affect the results presented here. Until about 2006, the drifter dataset was rather sparse, such that only a few patches of ocean were covered. Even in recent years, wide spatial gaps are prevalent (see, for instance, Figure 1c in Yu et al. (2019) and note that the y-axis scale is logarithmic). Therefore it is necessary to use all years of drifter observations in order to obtain global coverage that approximates what one obtains from just one year of output from a high-resolution model.

Drifter data are intrinsically Lagrangian, in contrast to the Eulerian model outputs to which they are compared. Nevertheless, segments of velocity time series from drifters can be used to estimate spectra and kinetic energy locally, yet keeping in mind that Lagrangian sampling leads to spectral smearing as drifters convolve spatial and temporal oceanic variability (Yu et al., 2019; Zaron & Elipot, 2021). For example, Lagrangian spectra have lower and wider tidal peaks, which do not stand above the background as much as peaks in Eulerian spectra do. In addition, tidal lines in both Lagrangian and Eulerian spectra widen due to interaction with currents and eddies, which pushes some of the tidal energy into a "non-phase-locked" (also referred to as "incoherent" or "nonstationary") component (e.g., Ray & Zaron, 2011; Shriver et al., 2014; Zaron & Egbert, 2014; Ponte & Klein, 2015; Kerry et al., 2016; Buijsman et al., 2017; Savage et al., 2017a; Zaron, 2017; Nelson et al., 2019).

We utilize both drogued and undrogued drifter data, in waters deeper than 500 m. Because the spatial and temporal distributions of the hourly drifter dataset are inhomogeneous (see for example Figure 1 of Yu et al. (2019) and Figure 1 of Elipot (2020)), we find it necessary to consider the entire dataset to properly define a global mean velocity field upon which local variance estimates depend. Examination of the drifter data geographical density per calendar month (not shown) do not indicate seasonal bias. Drogued drifter displacements, which comprise 48% of the trajectories in the hourly dataset version 1.04c, are expected to be representative of ocean velocity at 15-m depth with an estimated erroneous slip of the water past the drifter of 0.7 cm s^{-1} downwind per 10 m s^{-1} wind speed (Niiler & Paduan, 1995). Undrogued drifters, which comprise 52% of the dataset, are expected to represent ocean velocities at the surface (0 m), but with a slip of an order of magnitude larger compared to drogued drifters [8.6 cm s^{-1} per 10 m s^{-1} wind speed, (Lumpkin & Pazos, 2007)]. As such, undrogued drifter observations likely exhibit larger downwind velocity errors but these are yet to be comprehensively distinguished from real oceanic processes. For example, locally wind-driven velocities at the surface are more energetic than at 15-m depth because of vertical shear at a broad range of frequencies through Ekman dynamics (Elipot & Gille, 2009; J. M. Lilly & Elipot, 2021), or through surface gravity wave processes and their associated Stokes drift (e.g., Polton et al., 2005; Samelson, 2022). Yet, as will be seen throughout this paper, undrogued drifters qualitatively capture the same KE features as drogued drifters. A correction for the wind slip or an adequate assessment of its magnitude would need to be informed by an unknown dependency on frequency and to take into account the entire frequency spectrum of the observable wind forcing. In addition, typical estimation errors for the hourly drifter velocity estimates (Elipot et al., 2016) are between 2 and 5 cm s^{-1} (see Figure S2 of Yu et al., 2019) with unknown frequency distribution. As such, a comprehensive assessment of the velocity errors from drogued and undrogued drifters, and how these errors affect signal-to-noise ratios and kinetic energy estimates in various frequency bands, is beyond the scope of this study.

2.5 Analysis methods

Following Yu et al. (2019), velocity variance is estimated and interpreted as KE; no factor of 1/2 is included in the KE calculations. In order to study the distribution of KE as a function of time scale, we rely on estimating frequency rotary spectra (Gonella, 1972; Mooers, 1973) of velocity time series. Such spectra allow us to decompose velocity variance as a function of frequency, and to separate clockwise versus counterclockwise variances in order to distinguish anticyclonic energy from cyclonic energy.

To generally estimate velocity rotary spectra from models and drifters, complex velocity time series $u+iv$, where u and v respectively denote the zonal and meridional velocity components, are split into 60-day segments overlapping by 50%, detrended, and individually multiplied by a normalized Hann window to reduce spectral leakage. The discrete Fourier transform is then computed for all windowed segments and multiplied by their complex conjugates in order to obtain initial spectral estimates. To reduce computational time, model outputs are first subsampled on a $1/4^\circ$ grid before estimating spectra. Since we are using one-year model integrations, we can split each model velocity time series at each selected Eulerian grid point, and at each model depth (0 and 15 m), into 11 individual overlapping 60-day segments, discarding only a few days of data. Each segment is used to compute an initial spectral estimate, and the 11 resulting estimates are averaged to obtain a spectrum representative of the velocity variance for time scales of 60 days and shorter, at each individual location. This method should average the seasonality across the one-year model integrations, if present. These time-averaged spectra are further averaged in $1^\circ \times 1^\circ$ spatial bins before conducting subsequent analyses. Spatial averages are only computed when more than 50% of the points in a 1° by 1° bin are deeper than 500 m, and shallower gridpoints are discarded in the computation. For drifters, we divide up individual trajectories in as many 60-day overlapping segments as possible, discarding trailing data. For the dataset version 1.04c, we can obtain 174,803 60-day segments, 52,710 of which are from drifters with drogue on (drogued) and 108,861 are from drifters with drogue off (undrogued). This leaves 13,223 segments which are partly drogued and undrogued and are not considered to compute spectra.

In the next Results section, we consider zonally-averaged spectra (Figure 2). For the models, we simply calculate the average of all spectra within a given 1° latitude zonal bin. For the drifters, we average together the individual spectra for which the average latitudes of the corresponding segments are located within a given 1° latitude zonal bin. We also consider globally averaged spectra (Figure 3). For the models, we calculate a weighted average of all the $1^\circ \times 1^\circ$ spectra, where the weights are proportional to the surface area of the bins. For the drifters, we calculate weighted averages of individual initial spectra, separately for the drogued and undrogued drifters, where the weights are proportional to the cosine of the mean latitude of each corresponding segment. For both model and drifter globally-averaged spectra, we make sure to average spectra from anticyclonic frequencies together, and spectra from cyclonic frequencies together, the sign of which depends on the hemisphere of the data. For the drifters, we only consider trajectory segments for which the median of depths traversed along a segment is deeper than 500 m. Depths along drifter trajectories are obtained by interpolating the ETOPO1 global relief model (Amante & Eakins, 2009).

In order to produce maps of KE in specific frequency bands, we proceed as in Yu et al. (2019) for the models: the $1^\circ \times 1^\circ$ gridded rotary spectra are integrated over various frequency bands: semidiurnal ($\pm[1.9, 2.1]$ cpd), diurnal ($\pm[0.9, 1.1]$ cpd), high frequency (> 0.5 cpd and < -0.5 cpd), and near-inertial ($\pm[0.9, 1.1]f$, where f is the Coriolis frequency). Low-frequency KE is taken as total KE, computed as the time-mean of the squares of the zonal velocity time series plus the time-mean of the squares of the meridional velocity time series, minus high-frequency KE, the latter computed from the spectra.

To produce maps of KE from Lagrangian drifters in a specific frequency band, we do not integrate the drifter spectra as for the Eulerian models. Instead, for each band, we first apply a filter (bandpass or lowpass as needed) to the drifter velocity time series. In the near-inertial band, we apply a bandpass filter akin to the method of complex demodulation. The details of the bandpass filtering of the drifter data are given in the Appendix. Second, following bandpass filtering, we compute the variance of all filtered drifter velocities in $1^\circ \times 1^\circ$ spatial bins, independently of their drifter of origin. This new method based upon filtering differs from the study of Yu et al. (2019) in which band-specific variance estimates were calculated by firstly integrating the spectra of 60-day segment time series, secondly assigning the mean geographical positions of the segments to these estimates, and thirdly averaging them in 1° spatial bins to produce maps. The method employed in Yu et al. (2019) yields results similar to the ones presented here. However, our new method yields better spatial coverage in the drifter maps, especially near the equator, as well as slightly higher correlations between the drifter and model maps. Caution is warranted when interpreting the results for the near-inertial band. First, the near-inertial band as defined above covers only the "local" near-inertial KE. Near-inertial motions, such as low-mode internal tides, can propagate over long distances (Alford, 2003a; Simmons & Alford, 2012), and in such cases their frequency is no longer equal to the local value of f. Second, our analysis, like that of Yu et al. (2019), does not distinguish between near-inertial and diurnal motions where the definitions of these bands overlap, namely, within 24.1-37.5° of latitude.

We compare KE maps between depth levels by considering a proxy of vertical structure, namely the ratio of undrogued KE divided by the sum of undrogued and drogued KE for the drifters, and the ratio of 0 m KE divided by the sum of 0 m and 15 m KE for the models. This ratio statistic is preferable to a straightforward ratio of 0m to 15 m because it has an upper bound value of one when the KE at 15 m depth is zero. The ratio statistic is equal to 0.5 when the KE at 15 m is equal to the KE at the surface, greater than 0.5 when the KE at 15 m is less than at the surface, and less than 0.5 when the 15 m KE is larger.

Our comparisons of KE and ratio maps originating from drifters and models include Pearson correlation coefficients computed between maps. The statistical significance of each correlation estimate is assessed by drawing 1000 bootstrap sample pairs from which the standard error of the correlation is estimated. Using this method all non-zero correlations are deemed significant.

Finally, zonal averages of drifter and model KE maps and their ratio statistics are computed. Our plots of zonal averages display mean values and the standard error of the mean values computed over latitude bands.

3 Results

Zonally-averaged rotary spectra for undrogued and drogued drifters, and at 0 m and 15 m in the models, visualized as a function of frequency and latitude, display relatively similar KE levels and structures (Figure 2). Peaks corresponding to diurnal frequencies (near ± 1 cpd) and semidiurnal frequencies (near ± 2 cpd), and a large low-frequency continuum (near 0 cpd) are evident in all six subplots. Ridges of near-inertial energy, which follow the negative of the Coriolis frequency, from $\sim$ -1.7 cpd at 60°N to $\sim$ 1.7 cpd at 60°S, are also evident in all six subplots of Figure 2. Near 30° latitude, the inertial ridge overlaps with the diurnal peaks in the anticyclonic domain (at negative frequencies in the northern hemisphere, and positive frequencies in the southern hemisphere). The low-frequency peak, around zero cycles per day, is broader in frequency in the drifters than in the models. The models exhibit semidiurnal tidal peaks that rise above the background more dramatically than the peaks in the drifter spectra. The models also display a "peaky" or "picket fence" distribution of energy at high-frequency tidal harmon-

ics, with little energy in between the harmonics, as noted in previous studies (e.g., Müller et al., 2015; Savage et al., 2017b), which are likely caused by lack of the horizontal and vertical resolution required to spread energy from the peaks to a more continuous spectrum. In contrast, the drifter tidal peaks do not stand out above the background as strongly as in the models, as discussed earlier and in Zaron and Elipot (2021).

Another faint but striking feature of these latitude-frequency rotary spectra is the presence of translated images of the near-inertial ridge at $-f\pm1, 2, 3$ cpd in both drifter and model spectra. The model spectra additionally exhibit mirror images of the inertial ridge at $f\pm0, 1, 2, 3$ cpd. These features were previously seen in a similar figure in Yu et al. (2019) for drifters and MITgcm LLC4320, and for drifter data only in Elipot et al. (2016) up to 12 cpd. Elipot et al. (2016) speculated that these features may be representative of small departures from circular geometry for inertial oscillations, or of triad interactions between near-inertial waves and internal waves at tidal frequencies, but also noted that their magnitudes depended to some extent upon the processing applied to the drifter data to obtain hourly velocity estimates. The fact that these features are also observed in the models suggest that they might be representative of real, as yet unexplained, oceanic processes.

The relative energy levels in the different bands are more easily compared in globally averaged rotary spectra, for which the anticyclonic domain is assigned here to positive frequencies and the cyclonic domain to negative frequencies, using a southern hemisphere convention (Figure 3). The highest energy levels, associated with large-scale currents, mesoscale eddies, and Ekman flows, are seen in high and wide peaks at low frequencies (around zero). Whereas the near-inertial anticyclonic ridge is clearly visible in frequency-latitude spectra (Figure 2), in globally averaged spectra, that ridge is instead spread unevenly between 0 and 1.7 cpd in the anticyclonic frequency domain, weighted by the latitudinal distribution of the spectral estimates. As a result, energy levels are generally higher below the semidiurnal frequency band in the anticyclonic domain than in the cyclonic domain. Semidiurnal and diurnal peaks are clearly visible in both the model and drifter spectra but rise above the background much less in the drifter spectra than in the model spectra, as is made clear in the insets of Figure 3. The insets illustrate the wider and lower semidiurnal tidal peaks in Lagrangian spectra in comparison to Eulerian spectra. As noted earlier, in the higher frequency part (e.g., > 2 cpd) of the IGW continuum, spectra are much peakier in the models, especially HYCOM. The IGW continuum falls off more steeply in HYCOM than in MITgcm LLC4320, because of the lower resolution (coarser grid spacings) in HYCOM. The continuum is more elevated and smoother in the drifter spectra, and displays a noise floor at 12 cpd which is about one decade higher than MITgcm LLC4320, and more than two decades higher than HYCOM. This noise floor depends on the tracking-system for drifters. As shown by Yu et al. (2019), when only GPS-tracked drifters are considered instead of Argos-tracked drifters (Elipot et al., 2016), the spectral level and spectral slope at the highest frequencies for drifter spectra is in approximate agreement with MITgcm LLC4320 (see Figure 2 of Yu et al. (2019)). Many small but distinct spectral peaks that do not necessarily correspond to tidal constituents are seen in the drifter spectra for frequencies higher than 4 cpd. The amplitude and frequency of these peaks depend also on the drifter tracking system (see Figure 2 of Yu et al. (2019)) and may be artifacts of the estimation methods for drifter position and velocities (Elipot et al., 2016).

3.1 Low-frequency KE

Global maps of low-frequency KE highlight well-known large-scale currents and the mesoscale eddies they spawn, both of which are dominant in equatorial regions, western boundary current regions such as the Gulf Stream and Kuroshio, and the Antarctic Circumpolar Current (Figure 4, panels a-f). Ekman flows also contribute to these low-frequency KE patterns (Lumpkin & Johnson, 2013). At both depth levels, HYCOM over-

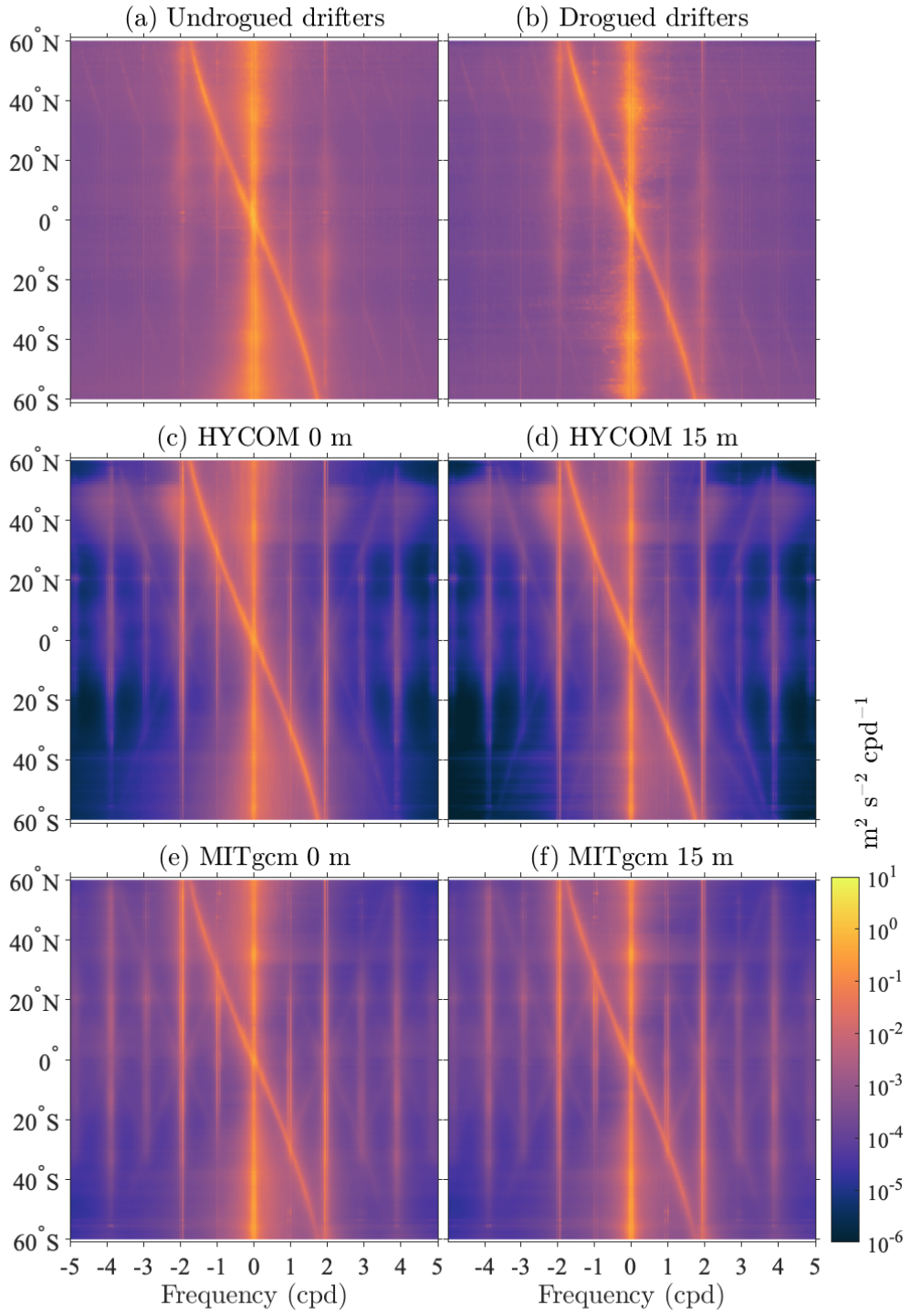

Figure 2. Zonally averaged rotary spectra of KE in 1° latitude bins between 60°S and 60°N for undrogued and drogued drifters (panels a and b), for HYCOM at 0 m and 15 m (panels c and d), and for MITgcm LLC4320 at 0 m and 15 m (panels e and f). Only frequencies between -5 and 5 cycle per day (cpd) are displayed. The frequency resolution is 1/60 cpd. The common decimal logarithmic color scale is displayed at the bottom right.

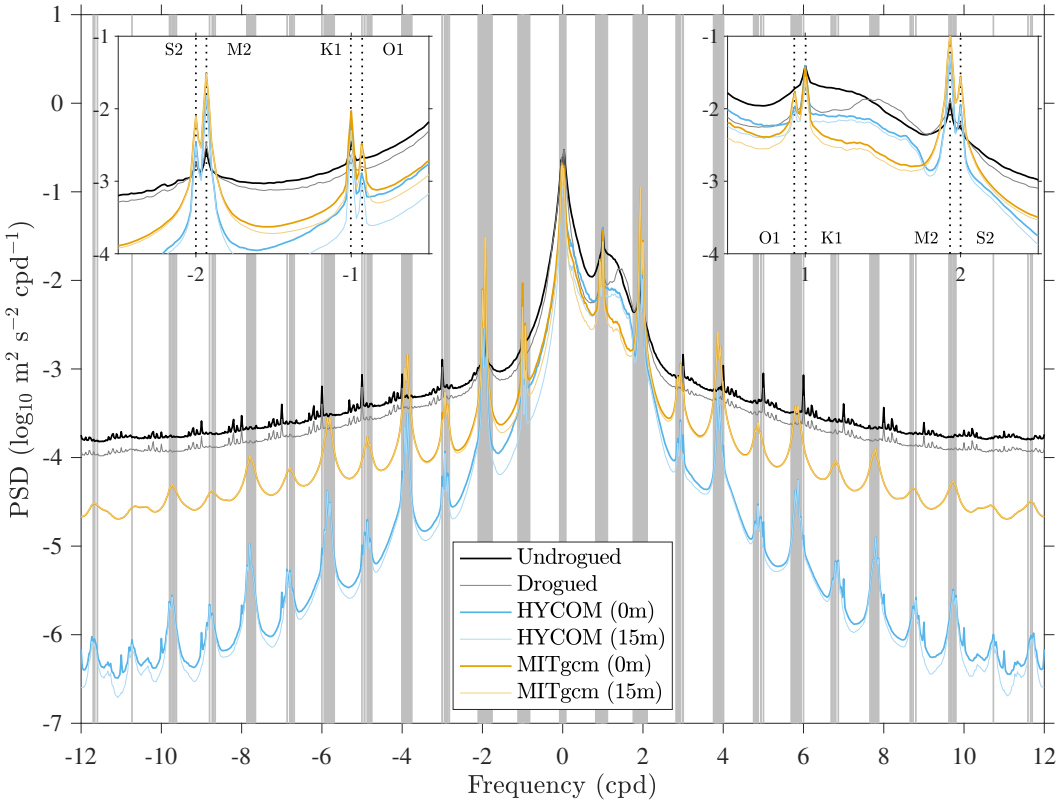

Figure 3. Globally averaged rotary spectra of KE from undrogued and drogued drifters (black and gray curves, respectively), from 0 m and 15 m HYCOM (thick and thin cyan curves, respectively), and from 0 m and 15 m MITgcm LLC4320 (thick and thin gold curves, respectively). Anticyclonic and cyclonic frequencies are assigned to positive and negative frequencies, respectively. The vertical gray lines indicate 145 tidal frequencies in both positive and negative frequency domains. The two insets show the same spectra but with a focus on diurnal and semidiurnal anticyclonic frequencies (right) and cyclonic frequencies (left). The vertical dotted lines in the insets show the O_1, K_1, M_2, and S_2 frequencies.

estimates the drifter observations in the near-equatorial southern Indian Ocean and in the Pacific off the Western coast of South America, while MITgcm LLC4320 overestimates the drifters in the eastern North Atlantic Ocean and parts of the Southern Ocean. MITgcm LLC4320 also features an incorrect positioning of the Gulf Stream, which does not veer to the northeast as it does in HYCOM and the drifters. The same Gulf Stream patterns were noted in surface velocities computed from satellite altimetry in Luecke et al. (2020). Despite these local differences, the spatial correlations between HYCOM and the drifters (0.76 and 0.77, for undrogued and drogued drifters, respectively) are comparable to, though slightly higher than, the correlations between MITgcm LLC4320 and the drifters (0.75 and 0.73, for undrogued and drogued drifters).

Maps of the low-frequency band vertical structure proxy ratio (Figure 4, panels g-i) display some clear similarities, despite the noisiness inherent in the drifter map. The mid- to high-latitude northeast and southeast Pacific Ocean, for instance, display similarly large values of the ratio (exceeding 0.5) in all three maps. In some specific locations such as near the equator in the Pacific, values of the ratio statistic slightly less than 0.5 are seen in both the model ratio maps and the drifter map. This suggests that some robust features of the oceanic circulation, both observed and modeled, are such that KE increases from the surface to 15 m depth. The spatial correlation between the model ratio maps (0.52) is higher than the spatial correlation between either model and the drifters. The HYCOM correlation with the drifter ratio map (0.48) is higher than the MITgcm LLC4320 correlation with the drifters (0.41).

Zonally averaged low-frequency KE in both models is generally comparable to, but lower than, drifter KE (Figure 5, panels a and b). The models and drifters all exhibit a peak of energy at the equator, but the peak values in HYCOM and especially MITgcm LLC4320 are too low, by a factor of about two. This disagreement between models and drifters near the equator should be interpreted with some caution as the sampling density from drifters near the equator is relatively low (see Figure 1(a) of Yu et al., 2019). HYCOM KE is too low across the mid- to high-latitudes of the southern hemisphere. With the exception of the energetic peak near 33°N, over most mid- to high-latitudes in the northern hemisphere, both models are too low.

The zonally averaged low-frequency band vertical structure proxy ratio in the models tracks the zonally averaged ratio in the drifters reasonably well (to within error bars) over most latitudes (Figure 5c). Maximum values of the ratio are seen at high latitudes in both hemispheres in the drifters and in HYCOM, whereas MITgcm LLC4320 does not track this high-latitude behavior. The greater energy in the undrogued drifters over most latitudes (represented by values of the ratio greater than 0.5) may be due in part to their wind bias as noted earlier. However, the relative closeness of this KE ratio in results from models, which do not suffer from a wind bias, to the drifter results suggests that wind bias alone is unlikely to account for all of the vertical structure seen in Figure 5c.

3.2 Near-inertial KE

Near-inertial KE is generally larger in mid-to-high latitudes than it is near the equator for both observational and model results, with the largest values found in the North Pacific (Figure 6, panels a-f), as shown in previous studies (e.g., Alford, 2003b; Chaigneau et al., 2008; Elipot et al., 2010). Faint but distinct relative maxima of KE are evident in the maps for the models around 30° where the diurnal and near-inertial bands overlap. MITgcm LLC4320 systematically underestimates the drifter results over most of the ocean, while HYCOM is in generally better agreement though it still underestimates the drifter results in the northern Pacific. Near-inertial KE is conspicuously lacking in MITgcm LLC4320 over the Antarctic Circumpolar Current south of 45°S. In both models, near meridional streaks of near-inertial KE stand out, probably related to individual tropical cyclones and storms present in the model forcing fields within their respective in-

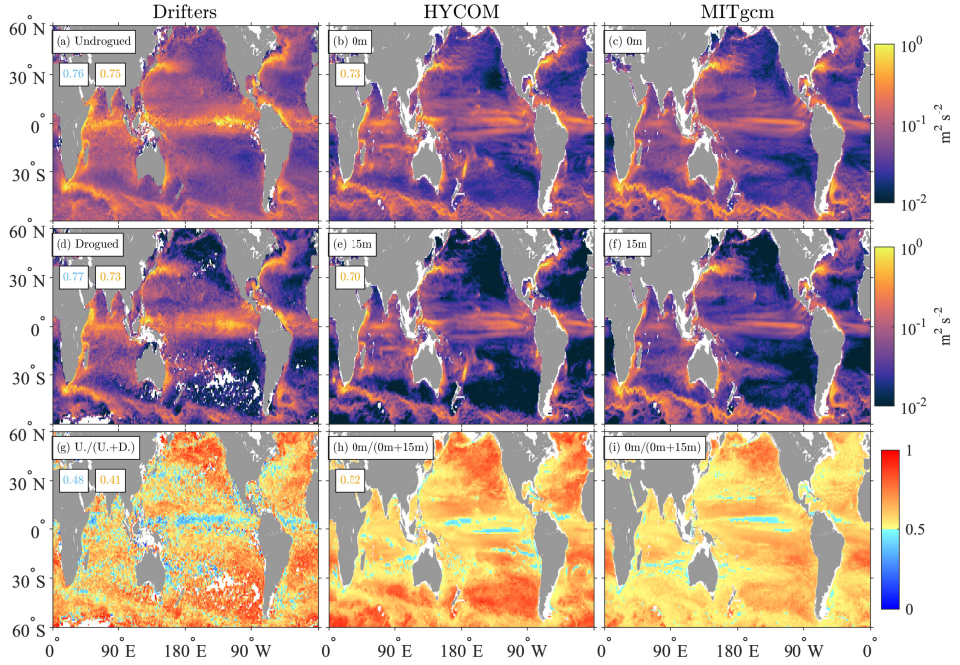

Figure 4. Global maps of low-frequency (> -0.5 cpd and < 0.5 cpd) kinetic energy (KE) from undrogued and drogued drifters (panels a and d), from HYCOM at 0 m and 15 m (panels b and e), and from MITgcm LLC4320 at 0 m and 15 m (panels c and f). The ratios of undrogued KE/(undrogued KE + drogued KE) for the drifters, and 0 m KE/(0 m KE + 15 m KE) for the HYCOM and MITgcm LLC4320 simulations, are shown in panels g, h, and i, respectively. The spatial correlations between the drifter maps and HYCOM and MITgcm LLC4320 maps are indicated in the upper left corners of panels a, d, and g, with HYCOM values in cyan to the left of MITgcm LLC4320 values in gold. The spatial correlations between HYCOM and MITgcm LLC4320 maps are indicated in the upper left corners of panels b, e, and h.

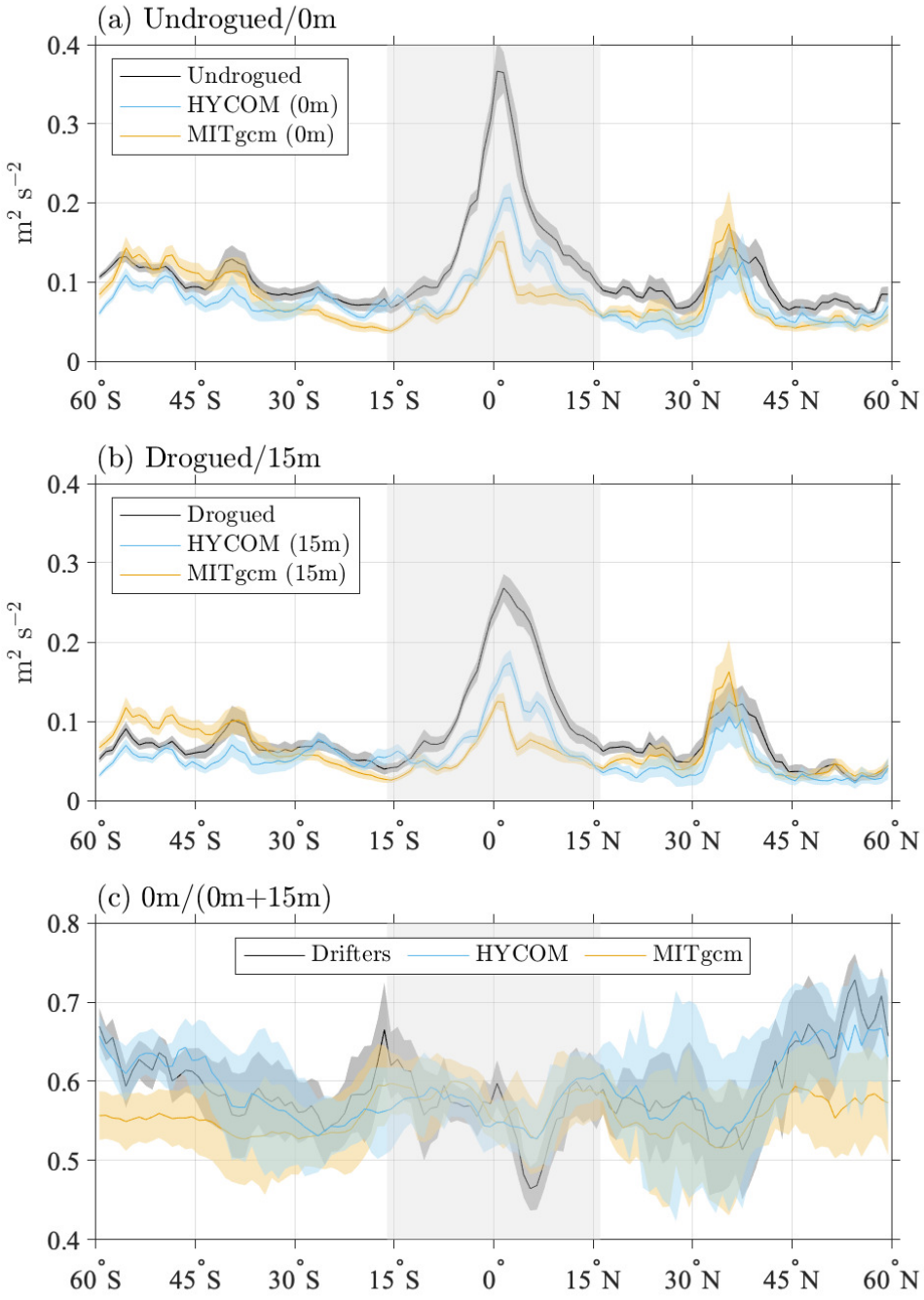

Figure 5. Zonally averaged low-frequency (> -0.5 cpd and < 0.5 cpd) kinetic energy (KE) from (a) undrogued drifters and 0 m model levels, and (b) drogued drifters and 15 m model levels. Zonal averages of undrogued KE/(undrogued KE + drogued KE) for the drifters, and 0 m KE/(0 m KE + 15 m KE) for HYCOM and MITgcm LLC4320, are shown in (c). The gray shaded region in each panel indicates the latitudes where the near-inertial and low-frequency bands exhibit some overlap (see Fig. 2). The shading around each curve corresponds to two standard errors of the calculated 1° zonal averages from the geographical maps.

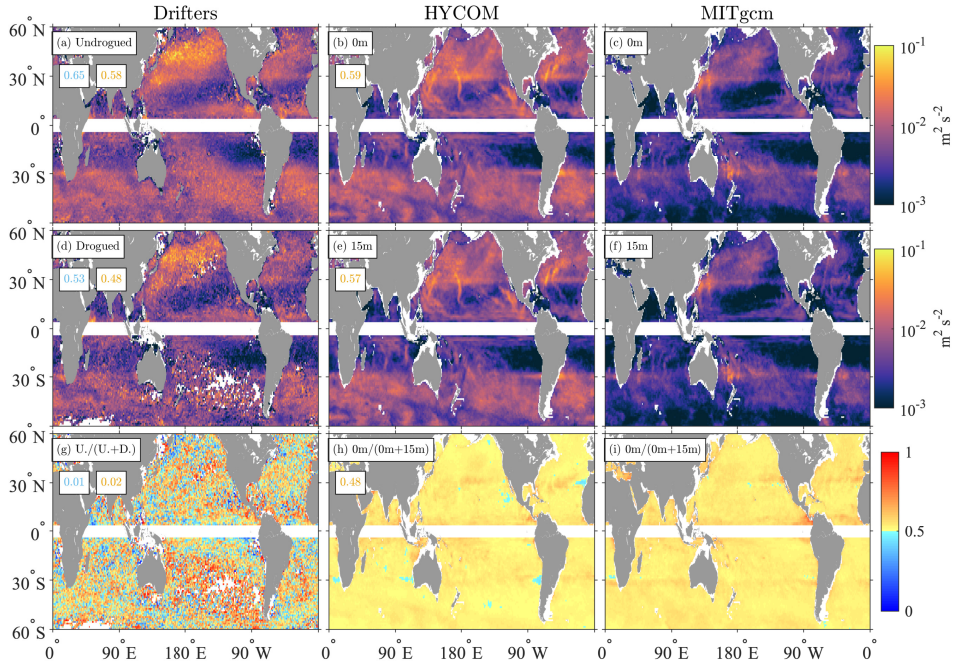

Figure 6. Global maps of near-inertial ($\pm[0.9, 1.1]f$) KE from undrogued and drogued drifters (panels a and d), from HYCOM at 0 m and 15 m (panels b and e), and from MITgcm LLC4320 at 0 m and 15 m (panels c and f). The ratios of undrogued KE/(undrogued KE + drogued KE) for the drifters, and 0 m KE/(0 m KE + 15 m KE) for the HYCOM and MITgcm LLC4320 simulations, are shown in panels g, h, and i, respectively. The spatial correlations between the drifter maps and HYCOM and MITgcm LLC4320 maps are indicated in the upper left corners of panels a, d, and g, with HYCOM values in cyan to the left of MITgcm LLC4320 values in gold. The spatial correlations between HYCOM and MITgcm LLC4320 maps are indicated in the upper left corners of panels b, e, and h.

tegration years. The drifter maps do not show such features which should be averaged out by the many years of drifter data used for this analysis. The different forcing years of the models and the multi-year nature of the drifter dataset may explain why the spatial correlations between these maps at both levels are lower than seen in, for instance, the low-frequency band; the two model maps correlate at 0.59 at the surface and at 0.57 at 15 m depth. The drifter maps correlate with the model maps at approximately equivalent levels, albeit slightly higher in HYCOM compared to MITgcm LLC4320 (0.65 versus 0.58 at the surface, and 0.53 versus 0.48 at 15 m).

The maps of near-inertial band vertical structure proxy ratio for the two models (Figure 6, panels h-i) appear similar but exhibit relatively low correlation between them (0.48). They both indicate that near-inertial KE is slightly larger at the surface compared to 15 m. Some unexplained discontinuities in these maps are noticeable near 30° latitude. The discontinuities may be due to overlapping dynamical processes of a different nature taking place there (tidal vs. wind-driven). The ratio map for the drifters (Figure 6, panel g) is noisy, and exhibits near-zero correlations with the model ratio maps.

In the zonal averages (Figure 7), as anticipated from the global maps, near-inertial KE is significantly higher in HYCOM than in MITgcm LLC4320. Near-inertial KE in HYCOM follows the drifters relatively well in the northern hemisphere between about 10-35°N and in the southern hemisphere. In the southern hemisphere, at the surface, the undrogued drifter near-inertial KE is however systematically slightly higher than HYCOM, perhaps because of underestimated windage of the undrogued drifters within strong wind environments. In contrast, at 15-m depth, HYCOM is in closer agreement with the drogued drifters between about 30-60°S. At latitudes between about 35-60°N, HYCOM KE values are closer to the drifters than MITgcm LLC4320 values are. However, over these latitudes HYCOM near-inertial KE is still substantially lower than drifter near-inertial KE. Separation of the zonal averages into basins demonstrates that the main cause of the discrepancy is located in the North Pacific Ocean (Figure 8).

The zonally averaged vertical structure proxy ratio for the near-inertial band is still noisy in the drifters, but is higher than 0.5 over most latitudes (Figure 7c). Over most latitudes, the model zonally averaged vertical structure proxy ratios follow the drifter ratios relatively well, within error bars. The model zonally averaged ratios are slightly larger than 0.5. Values between about 0.50-0.55, for instance, are typical.

3.3 Diurnal KE

The most energetic common spatial feature of the diurnal KE maps for the drifters, HYCOM, and MITgcm LLC4320 at both depth levels (Figure 9, panels a to f) corresponds to wind-driven near-inertial motions around $\pm 30°$ latitude. MITgcm LLC4320 therefore underestimates diurnal motions around these latitudes where diurnal and near-inertial motions overlap. Another common spatial feature is a global pattern associated with baroclinic tidal energy constrained equatorward of $\sim 30°$. The latter pattern is clearly seen in the models, but is less visible in the drifters because of the higher noise level in drifter data. MITgcm LLC4320 appears to overestimate the tidally-forced diurnal motions. Some faint but distinguishable diurnal KE features exist at both depth levels along the Agulhas Return Current and the Antarctic Circumpolar Current, in both models. These features are not as visible in the drifter maps, perhaps because of noise levels and poor sampling. The spatial correlations at both levels between models (0.76 and 0.75) indicate that the models capture similar KE patterns. At both depth levels, the spatial correlations between the drifter results and the model results suggest that HYCOM better captures the observations (0.78 and 0.85) than MITgcm LLC4320 does (0.55 and 0.67).

The maps of diurnal band vertical structure proxy ratio for the models (Figure 9, panels h and i) are generally similar, and exhibit a modest correlation between each other (0.56). The models display some modest correlation with the drifter ratio map (0.29 for HYCOM and 0.25 for MITgcm LLC4320). Similar patterns of relatively high proxy ratio values are visible in the equatorial regions and Southern Ocean, for both the drifter and model maps. The vertical structure proxy ratio is relatively low around $\pm 30°$. In this frequency and latitude band, KE is dominated by wind-driven near-inertial motions, which as discussed in the previous section have a measurable but small amount of vertical structure.

In the model results, we can separate the phase-locked (sometimes referred to as stationary or coherent) diurnal tidal motions from other diurnal motions using a tidal harmonic analysis, here of the two largest constituents (K_1 and O_1). Diurnal KE maps obtained from harmonic analysis, shown in Figure 10 (panels a to d), display enhanced regions near 30°, but these do not dominate the maps as dramatically as in Figure 9 because the wind-driven KE, which is not phase-locked, is not captured in the harmonic analysis. Substantial diurnal tidal KE regions are also noticeable equatorward of 30°, especially in the well-known diurnal tide hotspot in the western Pacific or along beams of baroclinic motions emanating from topographic features (Y. Wang et al., 2021); this

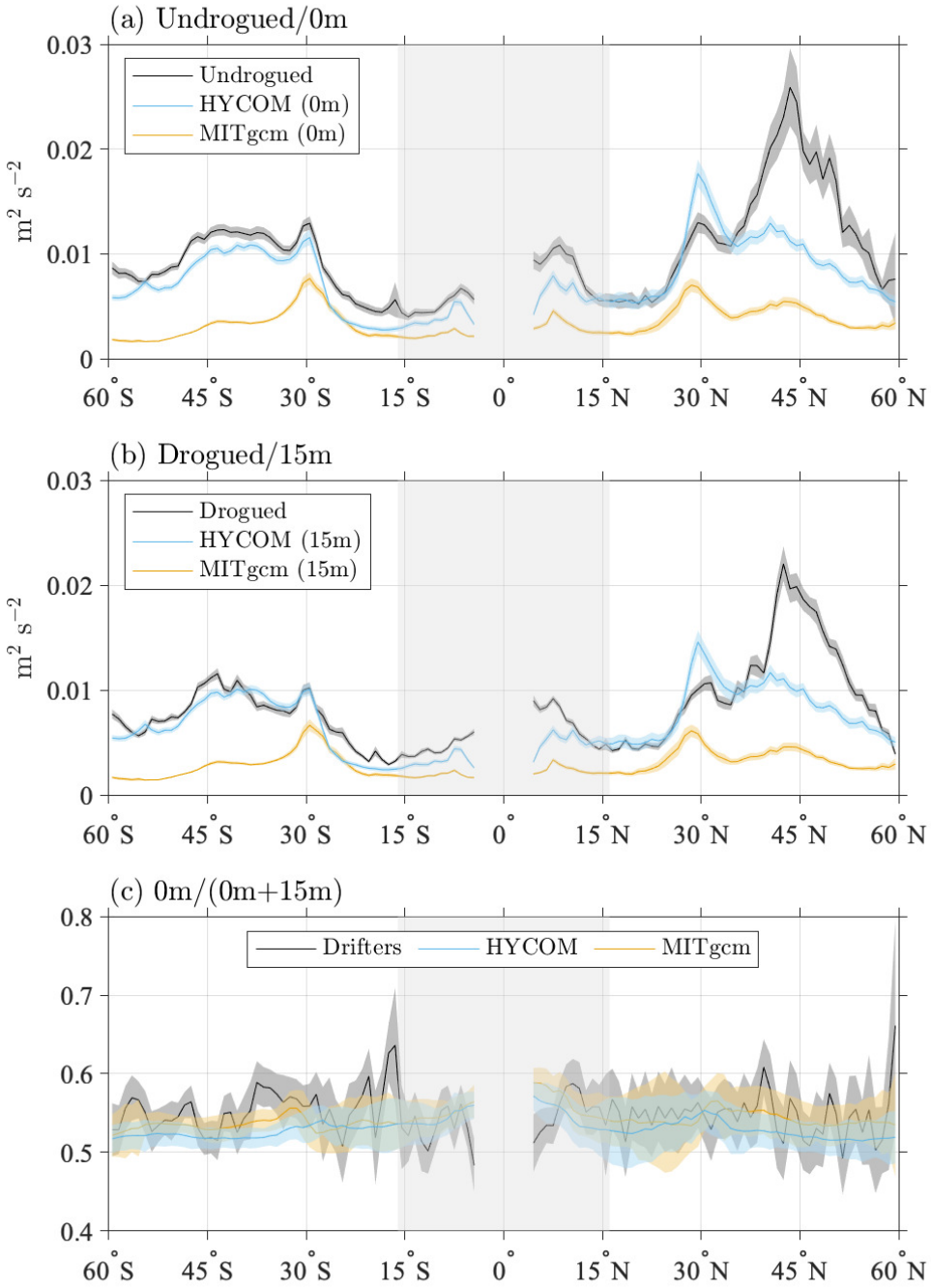

Figure 7. Zonally averaged near-inertial ($\pm[0.9, 1.1]f$) KE from (a) undrogued drifters and 0 m model levels, and (b) drogued drifters and 15 m model levels. Zonal averages of undrogued KE/(undrogued KE + drogued KE) for the drifters, and 0 m KE/(0 m KE + 15m KE) for HYCOM and MITgcm LLC4320, are shown in (c). The gray shaded region in each panel indicates the latitudes where the near-inertial and low-frequency bands exhibit some overlap (see Fig. 2). The shading around each curve corresponds to two standard errors of the calculated 1° zonal averages from the geographical maps.

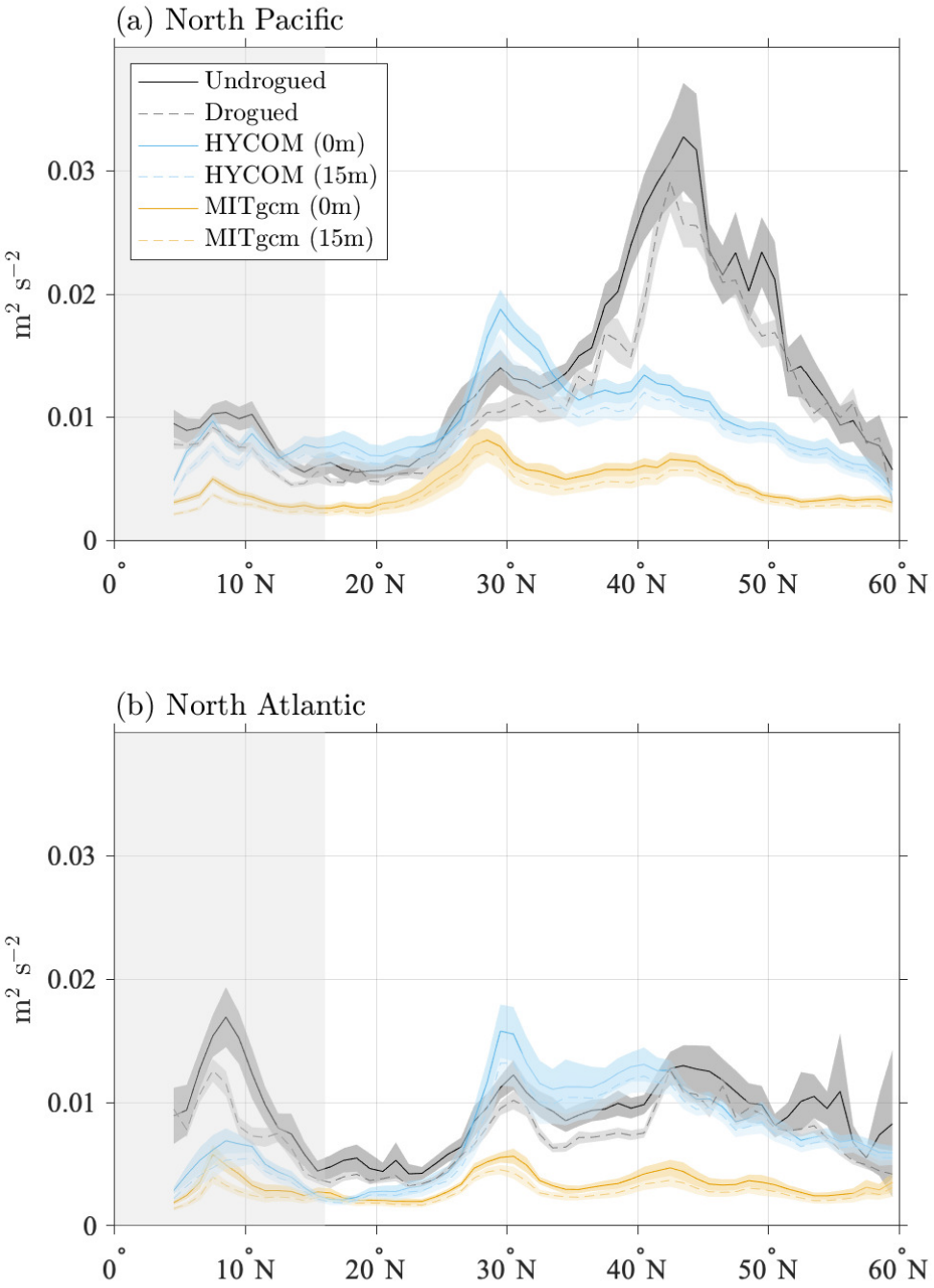

Figure 8. Zonally averaged near-inertial KE, as in Fig. 7a and b, but with North Atlantic and North Pacific Ocean basins examined separately. Note that in this figure, both undrogued/0 m and drogued/15 m results are displayed on both subplots.

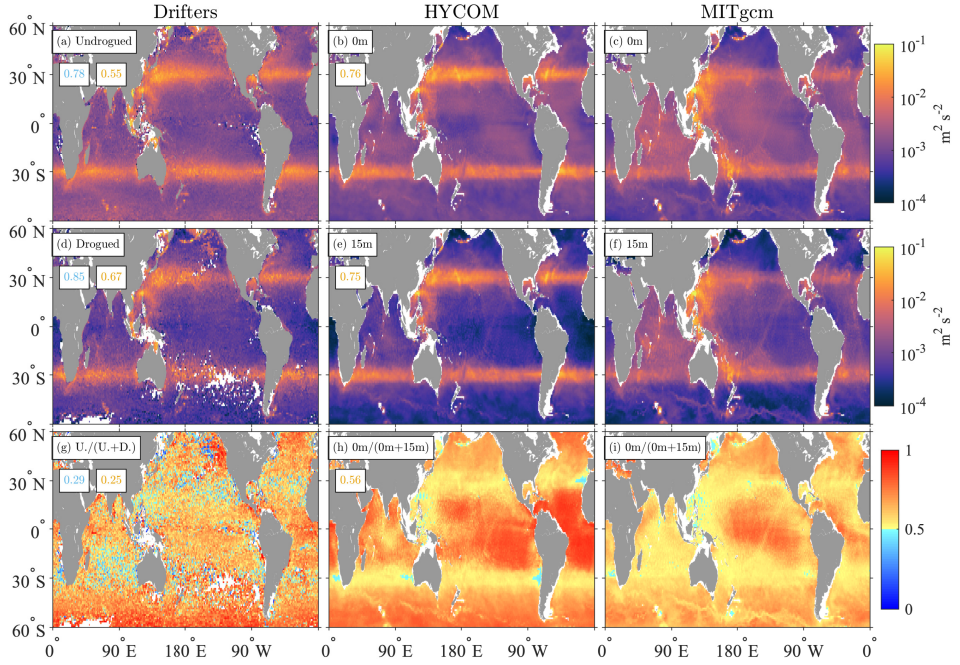

Figure 9. Global maps of diurnal ($\pm[0.9, 1.1]$ cpd) KE from undrogued and drogued drifters (panels a and d), from HYCOM at 0 m and 15 m (panels b and e), and from MITgcm LLC4320 at 0 m and 15 m (panels c and f). The ratios of undrogued KE/(undrogued KE + drogued KE) for the drifters, and 0 m KE/(0 m KE + 15 m KE) for the HYCOM and MITgcm LLC4320 simulations, are shown in panels g, h, and i, respectively. The spatial correlations between the drifter maps and HYCOM and MITgcm LLC4320 maps are indicated in the upper left corners of panels a, d, and g, with HYCOM values in cyan to the left of MITgcm LLC4320 values in gold. The spatial correlations between HYCOM and MITgcm LLC4320 maps are indicated in the upper left corners of panels b, e, and h.

location is also prominent in drifter data, e.g, Figures 9a and d. Except in specific locations such as the Sea of Okhotsk, Aleutian Island chain, the Campbell Plateau, and Kerguelen Plateau, diurnal KE computed from tidal harmonic analysis drops off steeply poleward of 30°, the cutoff latitude separating freely propagating from evanescent diurnal tidal motions. For both models, some diurnal KE is captured poleward of 30° by the harmonic analysis around some prominent topographic features in the Southern Ocean (for instance around the Kerguelen Plateau and the Campbell Plateau) or within the Alaskan Archipelago in the North Pacific. These features correspond to strong barotropic tidal currents, and some evanescent diurnal baroclinic tidal energy, unable to propagate far from their generation regions. The features seen in the total diurnal KE maps (e.g., Figures 9e-f) within the Agulhas Return Current and the Antarctic Circumpolar Current are absent in these harmonic analysis maps, suggesting that these are wind-driven in nature.

The vertical structure proxy ratio maps for the diurnal KE from the harmonic analysis (Figure 10, panels e and f) are complex. The ratios appear to be the result of superimposed long-wavelength patterns of barotropic tidal motions and short-wavelength patterns of baroclinic tidal motions within the tropical regions, and superimposed patterns of barotropic tidal motions and residual wind-driven motions at extratropical latitudes. The spatial correlations of the model diurnal KE maps (Figures 10a and c) from the harmonic analysis (0.82 for 0 m and 0.83 for 15 m) are slightly higher than for the total diurnal KE maps (0.76 and 0.75, for 0 and 15 m, respectively; Figures 9b and e). In contrast, the spatial correlation between models of the diurnal tidal ratio maps is lower (0.41, Figure 10e) than for the total diurnal KE ratio maps (0.56, Figure 9h).

Zonal averages (Figure 11) confirm that HYCOM lies closer to the diurnal peaks in the drifter results near 30°S and 30°N, while MITgcm LLC4320 diurnal energy is too weak in these peak regions. Equatorward of these peaks, MITgcm LLC4320 diurnal energy is generally too strong relative to drifter results, especially near 20°N, the latitude of the northwestern Pacific internal tide hotspot, while HYCOM KE is generally comparable to drifter values.

The zonally averaged diurnal band vertical structure proxy ratios in the models (Figure 11c) are complicated, as anticipated, and are revealing of model strengths and weaknesses. The drifter ratio is relatively high near the equator and at high latitudes. The MITgcm LLC4320 diurnal KE ratio follows the drifter ratio comparatively well over low- and mid-latitudes but is too low at high latitudes. The HYCOM diurnal KE ratio follows higher latitude drifter values more closely, and also follows the mid-latitude drifter ratio well, but is noticably higher than the drifter ratio over many latitudes equatorward of about 20°. Yet, recall that HYCOM tracks the absolute drifter KE values equatorward of 20° more closely than MITgcm LLC4320 does (panels a and b). The zonally averaged vertical structure proxy ratio for the diurnal tidal harmonic analysis KE lies relatively close to 0.5 over all latitudes. The relatively low ratios, and relatively low KE in the harmonically analyzed diurnal motions, suggests that phase-locked diurnal tidal motions are not a major contributor to the vertical structure of KE seen in the diurnal band. We will connect this to an analysis of vertical modes in the discussion section.

3.4 Semidiurnal KE

Global maps of semidiurnal kinetic energy (Figure 12, panels a to f) display known hotspots of semidiurnal internal tide motions near, for instance, Hawai'i, the French Polynesian islands, and the western Pacific. The KE values are substantially higher in the simulations, especially MITgcm LLC4320, than in the drifter observations. The hotspots are visible in the drifter maps, but less so because of the higher noise level in the drifter data. As highlighted in panels b and e, in HYCOM, the semidiurnal kinetic energy is spuriously large in a patch of the high-latitude North Pacific, south of the Aleutians, due

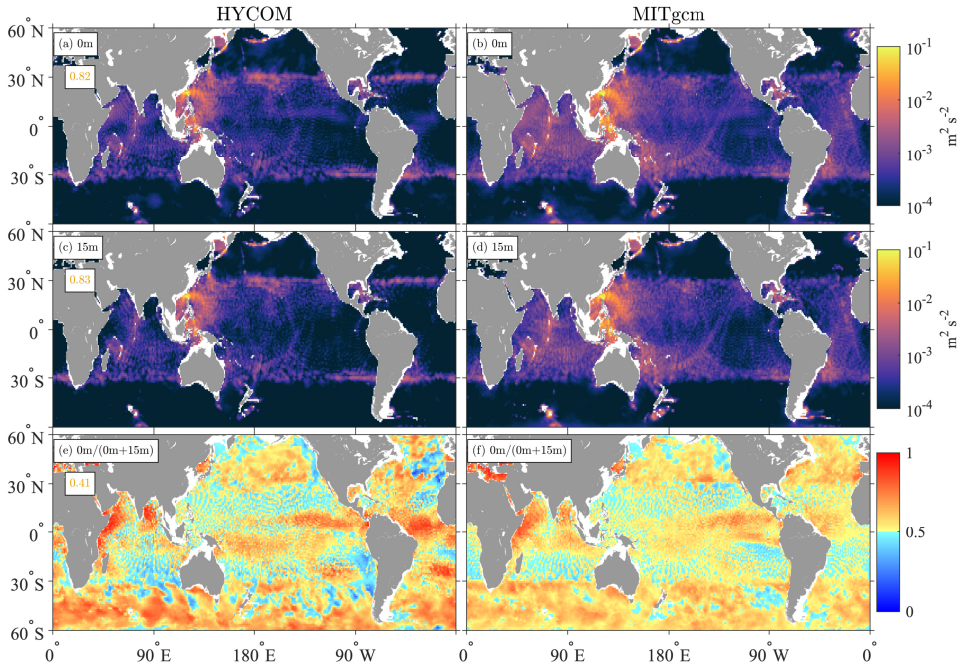

Figure 10. Global maps of diurnal KE calculated from harmonic analysis of diurnal tidal constituents K_1 and O_1 for HYCOM at 0 m and 15 m (panels a and c), and from MITgcm LLC4320 at 0 m and 15 m (panels b and d). The ratios of 0 m KE/(0 m KE + 15 m KE) for the HYCOM and MITgcm LLC4320 simulations are shown in panels e and f, respectively. The spatial correlations between HYCOM and MITgcm LLC4320 maps are indicated in the upper left corners of panels a, c, and e.

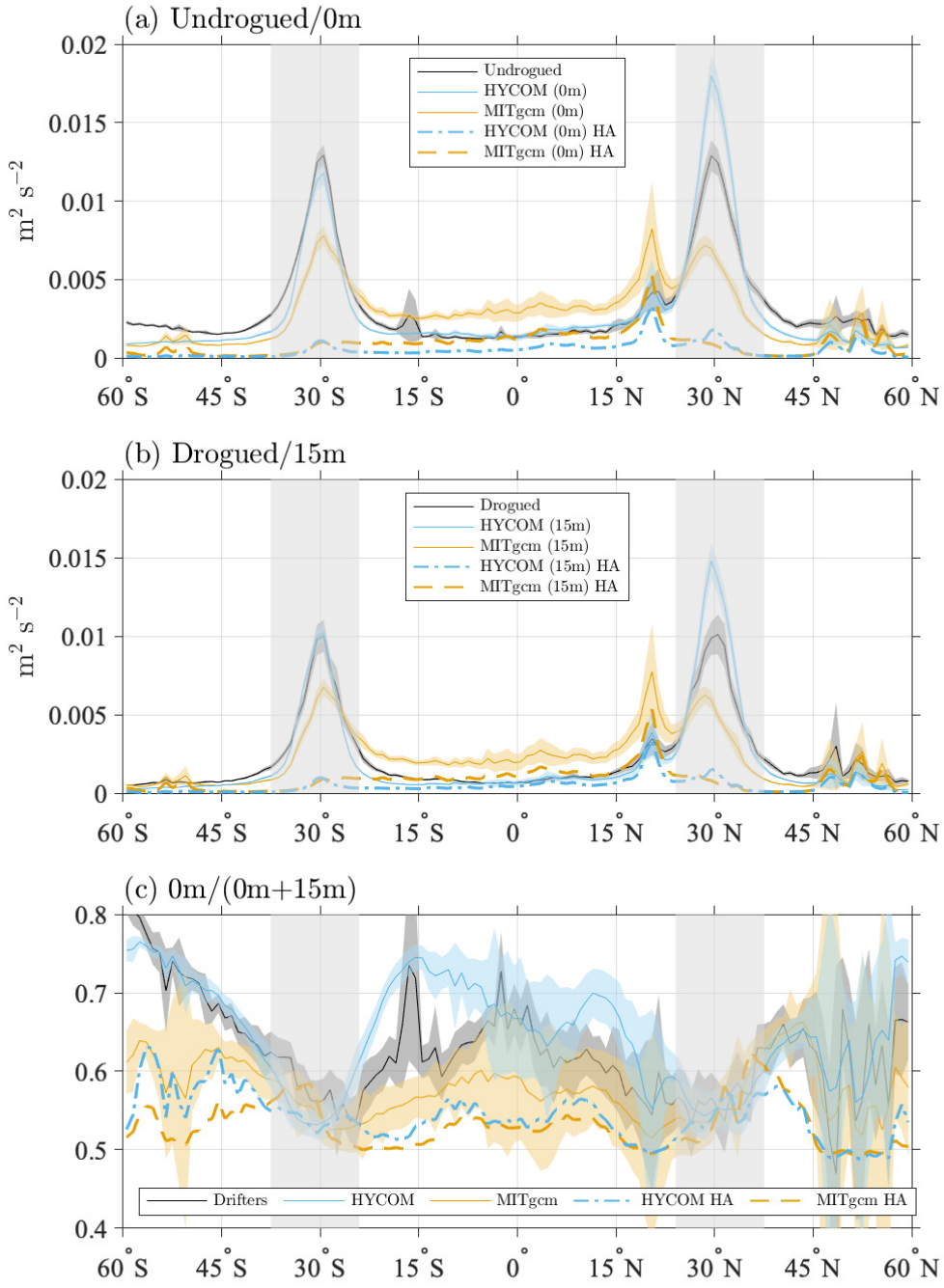

Figure 11. Zonally averaged diurnal ($\pm[0.9, 1.1]$ cpd) KE from (a) undrogued drifters and 0 m model levels, and (b) drogued drifters and 15 m model levels. Zonal averages of undrogued KE/(undrogued KE + drogued KE) for the drifters, and 0 m KE/(0 m KE + 15 m KE) in HYCOM and MITgcm LLC4320, are shown in (c). The zonally averaged diurnal KE from harmonic analysis ("HA", in legend) is also plotted for HYCOM (dash-dotted curve) and MITgcm LLC4320 (dashed curve). The gray shaded region in each panel indicates the latitudes where the diurnal and near-inertial frequency bands overlap (see Fig. 2). The shading around each curve corresponds to two standard errors of the calculated 1° zonal averages from the geographical maps.

to a known numerical instability (Buijsman et al., 2016). As is generally seen in other frequency bands, spatial correlations between model KE maps at both 0 and 15 m are higher (0.82 and 0.83) than the spatial correlations between either model KE map and the drifter KE maps, which range between 0.60 and 0.74. As in other frequency bands, spatial correlations between HYCOM and drifter semidiurnal KE maps are slightly higher than spatial correlations between MITgcm LLC4320 and drifter semidiurnal KE maps.

The vertical structure proxy ratio maps for the semidiurnal KE band differ substantially from ratio maps in other frequency bands. For both models (panels h and i), the ratio values are generally close to 0.5 indicating low differences of KE levels between the surface and 15 m. However, the spatial patterns are rather different, resulting in a modest correlation between the two model ratio maps (0.45). The ratio map for the drifters is again noisy (panel g), yet shows, as in the model maps, values closer to 0.5 than in other frequency bands. The spatial correlation between the drifter semidiurnal ratio map and the HYCOM semidiurnal ratio map is substantially larger than for MITgcm LLC4320 (0.28 compared to 0.10). This marked difference may be due to the ability of HYCOM to represent higher ratio values in the Southern Ocean and Gulf of Mexico, as is seen in the drifter observations. In the zonal averages (Figure 13, panels a and b), as demonstrated by Yu et al. (2019), MITgcm LLC4320 KE is higher than drifter KE over all latitudes, by a factor of up to four. Over most latitudes, HYCOM lies closer to the drifter KE than MITgcm LLC4320 does. A notable exception to this pattern is seen in northern hemisphere high latitudes, where the numerical instability in North Pacific HYCOM, mentioned earlier, is exhibited. The semidiurnal KE in HYCOM is still substantially larger than the drifter KE, in contradistinction to the closer agreement seen in comparisons of HYCOM internal tide SSH signatures with altimetry (Ansong et al., 2015; Buijsman et al., 2020). This illustrates the value of comparing models with velocity observations as well as SSH observations.

In contrast with results in other frequency bands, the vertical structure proxy ratios in the semidiurnal band are consistent with values of 0.5, to within error bars (Figure 13c), implying that there is on average no vertical structure in the semidiurnal band compared to the other bands. However, the large error bars on the drifter and model semidiurnal results may encompass the possibility of a small spatially-varying shear.

Motivated by the "wider and lower" semidiurnal tidal peaks in drifter spectra compared with model spectra (see insets of Figure 3), we examine in Figure 14 how the model vs. drifter semidiurnal zonal average comparisons change if the $\pm[1.9, 2.1]$ cpd semidiurnal band defined by Yu et al. (2019) is widened to $\pm[1.6, 2.4]$ cpd in incremental 0.1 cpd steps. As the definition of the semidiurnal band is widened, the drifter KE levels rise gradually, such that, over many latitudes, the agreement between HYCOM and drifters becomes fairly close for the widest definitions of the band (Figure 14, panels c and d). Again, the northern hemisphere high latitudes, where the numerical instability in North Pacific HYCOM is present, represent an exception to this pattern. Over most latitudes, MITgcm LLC4320 KE levels sit well above the drifters–typically by a factor of about two– for all definitions of semidiurnal band employed in Figure 14. By taking the wider nature of Lagrangian drifter spectra into account, these results suggest that the tidal currents in HYCOM may actually lie closer to the drifter values than the results in Figure 13 indicated.

4 Discussion

The difference in HYCOM and MITgcm LLC4320 near-inertial KE levels likely arises from the higher-frequency wind forcing in HYCOM (3 hours) vs. MITgcm LLC4320 (6 hours). Rimac et al. (2013) demonstrated that near-inertial KE in models is highly sensitive to the atmospheric forcing update intervals, with hourly forcing yielding KE three times higher than 6-hourly forcing. Flexas et al. (2019) found relatively low wind-power

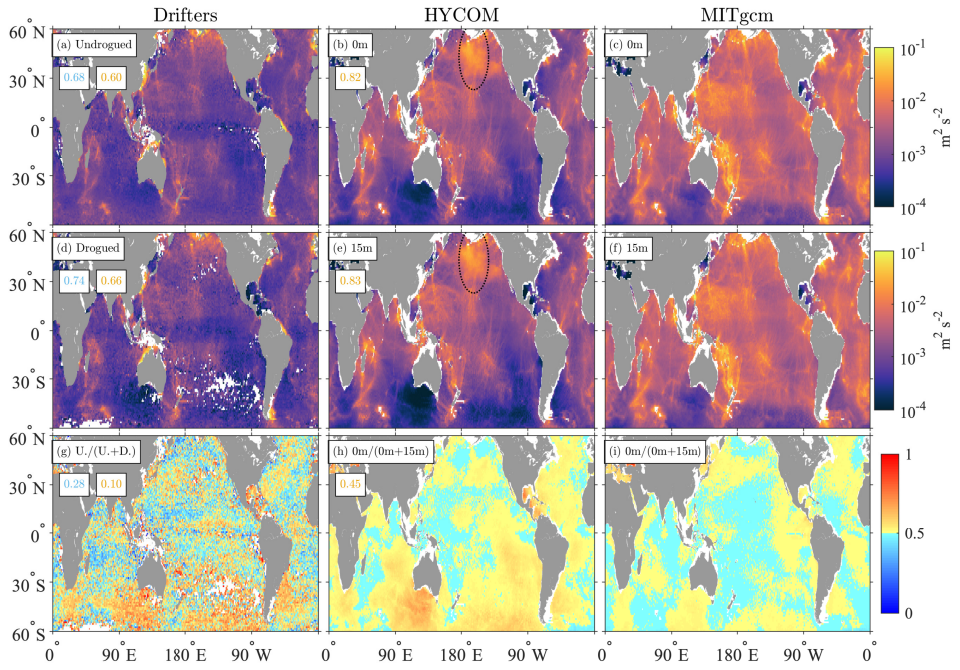

Figure 12. Global maps of semidiurnal ($\pm[1.9, 2.1]$ cpd) KE from undrogued and drogued drifters (panels a and d), from HYCOM at 0 m and 15 m (panels b and e), and from MITgcm LLC4320 at 0 m and 15 m (panels c and f). The ratios of undrogued KE/(undrogued KE + drogued KE) for the drifters, and 0 m KE/(0 m KE + 15 m KE) for the HYCOM and MITgcm LLC4320 simulations, are shown in panels g, h, and i, respectively. The spatial correlations between the drifter maps and HYCOM and MITgcm LLC4320 maps are indicated in the upper left corners of panels a, d, and g, with HYCOM values in cyan to the left of MITgcm LLC4320 values in gold. The spatial correlations between HYCOM and MITgcm LLC4320 maps are indicated in the upper left corners of panels b, e, and h. The North Pacific region of numerical instability in HYCOM (Buijsman et al., 2016) is indicated in panels b and e.

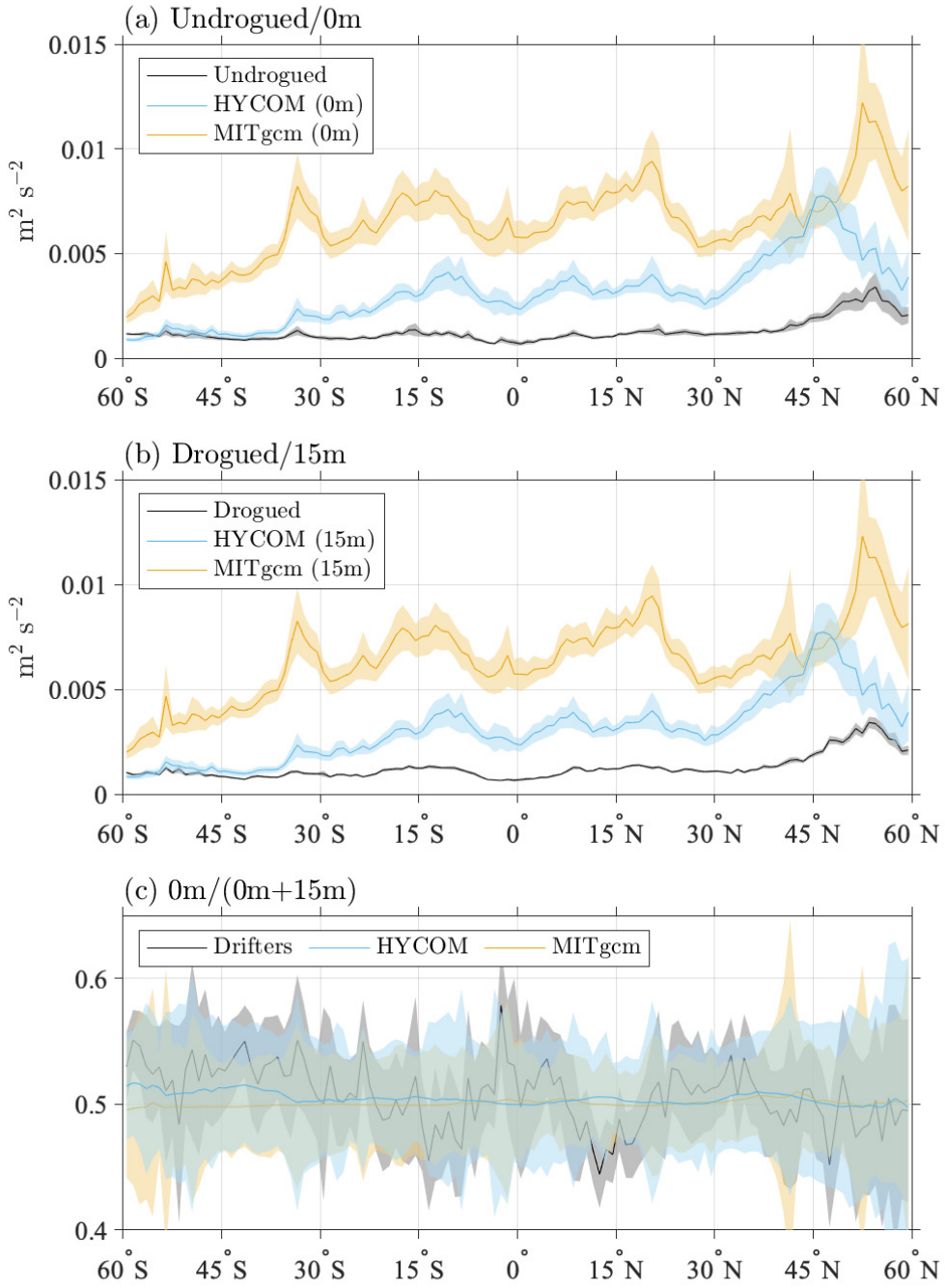

Figure 13. Zonally averaged semidiurnal ($\pm[1.9, 2.1]$ cpd) KE from (a) undrogued drifters and 0 m model levels, and (b) drogued drifters and 15 m model levels. Zonal averages of undrogued KE/(undrogued KE + drogued KE) for the drifters, and 0 m KE/(0 m KE + 15 m KE) for HYCOM and MITgcm LLC4320, are shown in (c). The shading around each curve corresponds to two standard errors of the calculated 1° zonal averages from the geographical maps.

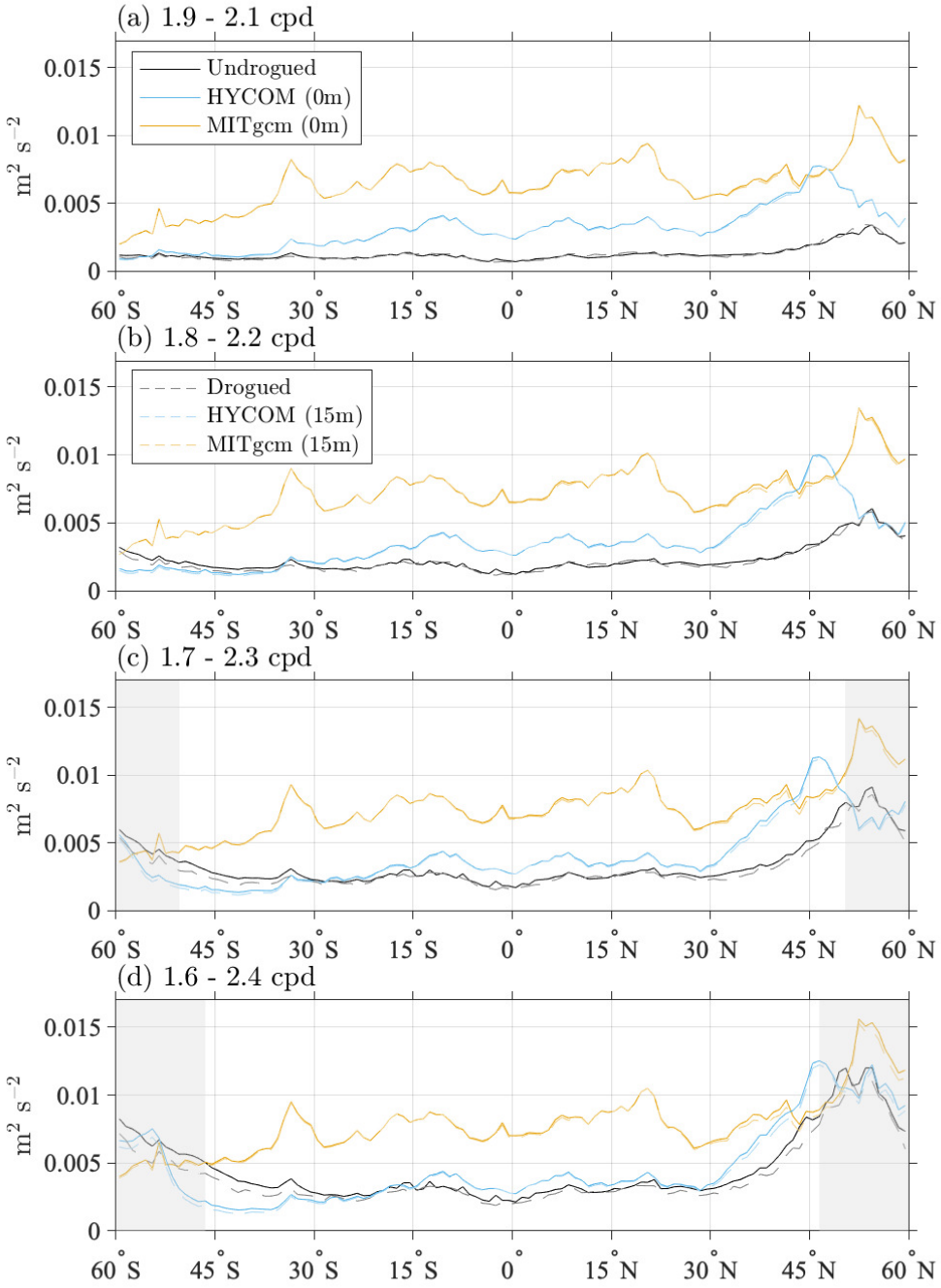

Figure 14. Zonally averaged semidiurnal KE estimates from drifters and model levels calculated by gradually widening the band of frequency integration from $\pm[1.9, 2.1]$ cpd to $\pm[1.6, 2.4]$ cpd as indicated in the title of each subplot. Uncertainty estimates are omitted here for clarity. In panels c and d, the gray shaded areas indicate the latitudes where the frequency bands of integration overlap with the near-inertial bands. The legend boxes in panels a and b are applicable to all panels.

input to the near-inertial motions in MITgcm LLC4320, due to the 6-hourly updates in the wind forcing. The HYCOM near-inertial KE, though higher than MITgcm LLC4320, is still too weak in the Pacific Ocean relative to drifter observations. Aside from insufficiently frequent atmospheric forcing updates, another potential cause of the model-drifter discrepancy in the near-inertial band is that the model outputs are of one year duration, while the drifter data span multiple years.

The largest discrepancy between models and drifter observations is in low-frequency flows at the equator; note the different y-axis scales in the low-frequency zonal average plot vs. the zonal average plots in other frequency bands. It is intriguing that HYCOM, with its more frequent atmospheric forcing, lies closer to the drifters in the equator than MITgcm LLC4320 does. The Intertropical Convergence Zone, or ITCZ, features rain and wind variability at high frequencies (sub-daily time scales) and small horizonal scales (Clayson et al., 2019; Thompson et al., 2019). This high-frequency wind and rain variability could potentially impact vertical momentum transfer into the ocean in the near-equatorial region. Thus, it is possible that atmospheric update intervals would make a difference to equatorial low-frequency dynamics as well as mid-latitude near-inertial dynamics. Fully probing the equatorial dynamics at work here is a subject for future research.

MITgcm LLC4320 has stronger diurnal tidal motions than HYCOM, probably because of the lack of parameterized topographic wave drag in MITgcm LLC4320. The wave drag in HYCOM is tuned for semidiurnal tides, not diurnal tides, which may as a result be over-damped in that simulation.

The model diurnal tide harmonic analysis KE values are significantly weaker than the model total diurnal KE values computed from integration of the frequency spectra in the diurnal band. This confirms that the diurnal band consists of motions other than phase-locked internal tides (non-phase-locked diurnal tides, diurnal jets and cycling of Ekman and submesoscale flows, and, in latitudes near 30°, near-inertial flow).

As indicated in Section 2.2, MITgcm LLC4320 had an overly large tidal forcing, and lacked the Self-Attraction and Loading (SAL) term, but these effects are not large enough to explain the discrepancy between MITgcm LLC4320 and drifter observations in the semidiurnal band. In future work, more direct comparisons of HYCOM and drifters, in which HYCOM is "seeded" with synthetic drifters, are warranted to investigate more comprehensively the biases introduced by the drifter Lagrangian sampling (Zaron & Elipot, 2021). If the closer agreement between HYCOM and drifters in the semidiurnal band holds up under further scrutiny, it would suggest, as in Ansong et al. (2015)'s analysis of internal tide SSH signals, that parameterized topographic wave drag (or some other plausible damping mechanism) is necessary for achieving agreement between semidiurnal tidal KE in models and observations.

The general agreement of the vertical structure proxy ratio in models and drifters, seen in spatial maps and zonal averages, supplies some confidence that the vertical structure proxy ratio computed from drifters is meaningful, noisy though it may be. Mode values of these ratios, for drifter observations and both models, over all frequency bands displayed in our 1° by 1° global maps, are given in Table 1. The global mode values are consistent with the presence of vertical structure in the low-frequency and diurnal bands, and, to a lesser extent, the near-inertial band. The semidiurnal band has less vertical structure, with most reported values being near 0.5.

To aid in interpreting the vertical structure of motions that are not directly wind-driven, such as diurnal tides, semidiurnal tides, and the low-frequency eddying general circulation (the latter arising indirectly from wind forcing), it is useful to compute the first three vertical modes (e.g., Gill, 1982; Arbic et al., 2018, among many), for semidiurnal, diurnal, and zero frequency (the latter representing the quasi-geostrophic limit). We use five different deep-ocean profiles in a US Navy climatology (Helber et al., 2013),

	Low-frequency	Near-inertial	Diurnal	Semidiurnal
Drifters	0.61	0.55	0.65	0.53
HYCOM	0.57	0.52	0.68	0.50
MITgcm	0.54	0.54	0.55	0.50

Table 1. Mode values of the ratio of undrogued KE/(undrogued KE + drogued KE) for the drifters, and 0 m KE/(0 m KE + 15 m KE) for HYCOM and MITgcm LLC4320, in four different frequency bands. A value of 0.5 indicates that the KE is the same at the two depth levels.

at 10°S, 206°E and at four different latitudes (50°N, 10°N, 6°N, and 50°S) along 210°E. The values of the vertical structure proxy ratio computed from these low vertical modes are greater than 0.5, but only by small amounts (ranging from 0.5000-0.5012), less than the near-inertial values seen in Figure 7c and much less than the low-frequency and total diurnal values seen respectively in Figures 5c and 11c. The low vertical structure proxy ratios in the vertical normal mode analysis are consistent with the lack of vertical structure seen in our semidiurnal results and diurnal tidal harmonic analysis results, both of which are almost entirely due to tidal motions. Semidiurnal and especially diurnal tidal currents do have a surface-intensified profile (Timko et al., 2013, their Figure 5), but this surface intensification takes place over vertical scales that are significantly larger than 15 m.

The lack of vertical structure between 0 and 15 m in the low vertical mode analysis is inconsistent with the vertical structure proxy values exceeding 0.5 in the low-frequency and diurnal band results. Additional physics, such as wind-driven Ekman and other motions, is taking place in the diurnal and low-frequency bands (and in the near-inertial band). As discussed in Section 2.3, motions that are directly wind-driven are expected to exhibit some vertical structure in the upper ocean. The proxy ratio values greater than 0.5 in the diurnal band results (Figure 11c) are likely due to non-tidal effects, such as near-inertial flows (in latitudes where they overlap), diurnal jets and cycling in Ekman flows (Price et al., 1986; Price & Sundermeyer, 1999; Sutherland et al., 2016; W.-Y. Sun & Sun, 2020; Masich et al., 2021), and diurnal cycling in submesoscale flows (D. Sun et al., 2020). Regarding the latter possibility, however, we note that the grid spacings in the global models examined here are not sufficient to fully resolve submesoscale eddies (Capet et al., 2008). A detailed study of the combined effects of tidal and wind forcing on velocities and temperatures in the diurnal band in a specific region can be found in Aristizábal et al. (2016).

The "interior quasi-geostrophic" component (Lapeyre & Klein, 2006) of low-frequency large-scale currents and mesoscale eddies is dominated by barotropic and low baroclinic modes (Wunsch, 1997), or, in an alternative view, by a "surface mode" that is strongest at the surface and approaches zero flow at the seafloor (LaCasce, 2017), due to the influence of bottom topography (LaCasce, 2017) and/or bottom and topographic wave drag (Arbic & Flierl, 2004; Trossman et al., 2017). The surface mode described by LaCasce (2017) decays with depth at the ocean surface, as do the traditional low baroclinic modes. In addition, low-frequency motions may also have a substantial "surface quasi-geostrophic" component (Lapeyre & Klein, 2006; LaCasce & Wang, 2015), which is surface intensified and may therefore contribute to the weaker motions at 15 m depth relative to the surface. However, the simplest explanation for the proxy ratio values greater than 0.5, seen in the low-frequency band (Figure 5c), is that they are due to Ekman flows, which exhibit substantial variation over short vertical scales (Elipot & Gille, 2009; J. M. Lilly & Elipot, 2021).

5 Summary and conclusion

Near-surface ocean kinetic energy (KE) is an important factor in a variety of problems, including but not limited to air-sea interaction, pollution transport, and satellite mission planning. Such applications require better quantification and understanding of the space-time variability of near-surface oceanic KE, including its frequency dependence and vertical structure (Elipot & Wenegrat, 2021).

We have compared the KE in two widely used global high-resolution general circulation simulations (HYCOM and MITgcm LLC4320) to drifter observations. We compare the sea surface (0 m) KE in the models to KE from undrogued drifters, and the KE at 15 m depth in the models to KE from undrogued drifters. We also compare a vertical structure proxy ratio, computed from 0 m KE/(0 m KE + 15 m KE) in the models and from undrogued KE/(undrogued KE + drogued KE) in the drifter observations. We compare the KE and the vertical structure proxy ratio across a wide range of frequencies, enabled by new drifter technologies and analyses that allow for high-frequency mapping, and by the inclusion of astronomical tidal forcing and relatively high atmospheric forcing updates in HYCOM and MITgcm, that activates tidal and near-inertial flows alongside lower-frequency flows such as Ekman flows and the eddying general circulation.

Our goal is a descriptive paper focused on global maps of KE and the vertical structure proxy ratio. The uniqueness and computational cost of the simulations used here prevent us from conducting sensitivity analyses for the comparison to observations. The drifter dataset as well is unique and quite different in nature from the models, meaning that some of the comparisons made here are not as "apples-to-apples" as one might have preferred. Some inconsistencies between analyses of the models and drifters, and examples of important contributing processes that should be examined in more detail, are listed below:

- Generating robust statistics and geographical coverage from drifter data requires us to use many years of observations. We use more than 30 years here.
- At the same time, the computational expense of the simulations, and the fact that they are run at different centers with no coordination between them, requires us to use a small number of years, and makes it difficult to use the same year from each model simulation. We use one year of output from the HYCOM and MITgcm LLC4320 simulations–with start dates of 1 January 2014 and 12 November 2011, respectively.
- The KPP parameters, which exert strong control on vertical structure, differ between the two simulations.
- The vertical grid resolution also differs between HYCOM and MITgcm LLC4320.
- The atmospheric products used to force the two simulations are different, and their update frequency is different (3-hourly NAVGEM for HYCOM, 6-hourly ECMWF for MITgcm LLC4320).
- The model results are Eulerian, whereas the drifter results are Lagrangian.
- The frequency dependence of the noise in the drifter observations, in particular the undrogued drifters, is not yet characterized.
- We do not examine the important topic of seasonality.
- The MITgcm LLC4320 simulation had a few mistakes in the tidal forcing, and did not employ a parameterized topographic wave drag as HYCOM did.

Our study follows that of Yu et al. (2019), who used only MITgcm LLC4320 but whose study otherwise likewise suffered from all of the problems noted above. The three-way comparison between drifters and two models allows us to assess the strengths and weaknesses of all three products. Following Yu et al. (2019), who compared KE in the MITgcm LLC4320 simulation to drifters, we find that near-inertial motions in MITgcm

LLC4320 are too weak while semidiurnal tidal motions are too strong. Here we find that the HYCOM KE values lie closer to the drifters in both the near-inertial and semidiurnal tidal bands, but for different reasons. In the near-inertial band, HYCOM is stronger than MITgcm LLC4320 due to more frequently updated atmospheric forcing fields. In the semidiurnal tidal band, HYCOM is weaker than MITgcm LLC4320, due primarily to the parameterized topographic internal wave drag, which simulates the energy lost due to unresolved wave generation and breaking processes, and which is employed in HYCOM but not in MITgcm LLC4320. While HYCOM semidiurnal tidal KE lies closer to the drifters than MITgcm LLC4320 KE does, the HYCOM semidiurnal KE is still stronger than the drifter KE if the Yu et al. (2019) definition of the semidiurnal band is employed. However, if we widen the definition of semidiurnal band from that employed in Yu et al. (2019), the HYCOM tidal KE lies closer to the drifters over most latitudes, while MITgcm LLC4320 semidiurnal KE is too high. Widening the definition of the semidiurnal band to accommodate comparisons to drifters may be justified, due to the inherently "wider" nature of Lagrangian spectra relative to Eulerian spectra (Zaron & Elipot, 2021). To be more sure of this interpretation, both HYCOM and MITgcm LLC4320 could be seeded with numerical particles and the resulting Lagrangian velocity spectra could be more directly compared to drifter spectra from the actual ocean. This computationally expensive undertaking is left as a topic for future investigation.

Our conclusion that damping parameterizations are necessary for attaining realistic semidiurnal tidal kinetic energy levels is consistent with the results of Ansong et al. (2015). The latter paper demonstrated that the sea surface height signature of internal tides in HYCOM is closer to altimetry observations when the HYCOM simulations contain a wave drag than when they do not. The work here, comparing HYCOM and MITgcm LLC4320 simulations with drifter observations, suggests that the lack of parameterized wave drag in LLC4320 leads to overly large tidal kinetic energies. Indeed, the contrast between simulations with and without wave drag is greater for tidal kinetic energy than it is for internal tide sea surface height. Some caution regarding this interpretation is warranted, however, as we are comparing two different models.

The diurnal band is complicated because of overlapping processes. Diurnal motions include diurnal tides, diurnal jets and cycling of Ekman and submesoscale flows, and, in latitudes where the frequency-band definitions overlap ($\sim 30°$), near-inertial flows. The phase-locked component of diurnal tides can be computed separately from other diurnal motions via a tidal harmonic analysis. Maps and zonal averages indicate that phase-locked diurnal tides are a relatively small component of the KE seen in the diurnal band.

In additional results, we have shown that HYCOM lies closer to drifters in the diurnal band (with the notable exception of the vertical structure proxy ratio at low latitudes), that low-frequency (<0.5 cpd) motions in both models are generally too weak, especially near the equator, that both models suffer from weak near-inertial motions in the northern mid-to-high latitudes, and that numerical instabilities yield overly large tidal HYCOM semidiurnal KE in the North Pacific.

HYCOM has higher spatial correlations with drifter KE than MITgcm LLC4320 does, across a wide variety of frequency bands. This result is consistent with Luecke et al. (2020)'s finding that the spatial correlations between HYCOM and mooring observations of KE and temperature variance are higher than the correlations between MITgcm LLC4320 and mooring observations.

With some exceptions, in the maps and zonal averages, the models capture the latitude- and frequency- dependence of the vertical structure proxy ratio relatively well. The low-frequency, near-inertial, and diurnal bands display significant vertical structure, while the semidiurnal band shows little vertical structure. Ekman flows, and their diurnal cycling, likely explain some of the vertical structure seen in the low-frequency and diurnal bands.

The broad approach employed here has left us with several unsolved problems and questions. For instance, the near-surface KE in the diurnal band, which is forced by the astronomical tidal potential and the diurnal solar heating cycle, requires much more examination than we provided here. The large differences between low-frequency equatorial flows in the models and drifter observations represent a first-order problem for future work. In addition, the vertical structure of the upper ocean velocities throughout the entire mixed layer (not just at 0 and 15 m), and the sensitivity of these velocities to the vertical grid spacing and KPP parameters, is another topic that deserves more attention. The geographical and frequency dependence of upper ocean flows and their vertical structure is indeed a rich topic for research.

Appendix A Drifter velocity filtering

To filter the drifter velocity time series and eventually obtain KE maps, we consider all trajectories of the drifter hourly dataset (version 1.04c) that are 4-day long and longer. We have chosen a time series filter which is a continuous wavelet transform using a generalized Morse wavelet (J. M. Lilly, 2017). For the diurnal and semidiurnal cases, to achieve a bandpass filter, the frequency spectrum of the generalized Morse wavelet is chosen to be centered on the middle frequency of the desired frequency band (1 and 2 cpd for the diurnal band and semidiurnal bands, respectively), and the half-power bandwidth of the wavelet spectrum is set to approximately match the desired interval for the bandpass ([0.9, 1.1] cpd and [1.9, 2.1] cpd for the diurnal and semidiurnal bands, respectively). Following the notation of J. M. Lilly and Olhede (2012), such characteristics of the wavelet are achieved by setting the Morse wavelet parameter γ to 3, and the parameter β to $(\nu/\Delta\nu)^2/\gamma$ where ν is the center frequency of the frequency-domain wavelet in each case, while $\Delta\nu$ is its half-power bandwidth (0.1 cpd in our case). Such calculation of the wavelet parameters however relies on a quadratic approximation of the frequency-domain wavelet to determine the half-power point frequencies. Practically, this wavelet transform and filtering method is implemented with the function `wavetrans` of the Matlab toolbox jLab (J. M. Lilly, 2021). An online course describes this specific method of using the wavelet transform as a narrow bandpass filter (J. M. Lilly, 2022).

For the low-frequency band, in contrast to the approach used for the models, we explicitly lowpass the drifter velocities before calculating the variance in spatial bins. This lowpass variance is added to the mean velocity field squared to obtain the low-frequency KE. The lowpass filter is also achieved here by using a wavelet transform, but by setting the Morse wavelet parameters γ to 3 and β to 0, and by setting the half-power point frequency to 0.5 cpd (J. Lilly & Olhede, 2009, section IV. A.).

For the near-inertial band, we also apply a wavelet transform method, but one that continuously changes the center frequency of the wavelet to follow the local inertial frequency as the drifter latitude changes. This specific method is now coded in the function `inertialextract`, also part of the Matlab toolbox jLab (J. M. Lilly, 2021). The function is used by specifying the wavelet duration parameter $P = \nu/\Delta\nu$. With $\nu = -f$ and $\Delta\nu = -0.1f$, we obtain $P = 10$. The function is implemented by passing as arguments the times, longitudes, and latitudes of a drifter trajectory. The function calculates the local inertial frequency based on the latitude, and subsequently returns the instantaneous complex-valued inertial oscillation amplitudes in kilometers. These displacement amplitude time series are subsequently differentiated with respect to time to estimate the corresponding near-inertial velocities, using a central difference scheme. Because the wavelet transform operation implemented in `inertialextract` is analytic, it filters the energy only on one side of the frequency domain, whichever one corresponds to the anticyclonic side, depending on the sign of the latitude. Because we are seeking to extract the KE not only around the inertial, anticyclonic, frequency $(-f)$, but also around its opposite, cyclonic, frequency (f), the function `inertialextract` is applied a second time by negating the longitude time series of each drifter. This amounts to a

complex conjugation of the time series, which interchanges the cyclonic and anticyclonic sides of the spectrum. As for the model analyses, the spatial variance of the anticyclonic and cyclonic frequencies are summed to obtain the total near-inertial KE. Conceptually, this method is equivalent to the method known in oceanography as complex demodulation (Emery & Thomson, 2001) but with the use of a filter that is specifically chosen for its property of analyticity; see e.g. (J. Lilly & Olhede, 2009), Section IIB for a discussion of the importance of this property.

Appendix B Open research

This paper uses software made available by the Pangeo project, by jLab (J. M. Lilly, 2021) and by the "cmocean" package (Thyng et al., 2016). MITgcm LLC4320 output is available at `https://data.nas.nasa.gov/ecco/data.php?dir=/eccodata/llc_4320`. The surface drifter data are available at `https://www.aoml.noaa.gov/phod/gdp/hourly_data.php`. HYCOM output can be accessed via the OSiRIS infrastructure. Co-authors B.K.A. and J.F.S. can be contacted for details on OSiRIS access. The Matlab code used to process the MITgcm LLC4320 and HYCOM outputs into the results used in this paper, the results from MITgcm 4320, HYCOM, and processed drifter data, and the code used to produce all of the plots in the paper, are provided in Arbic et al. (2022); `https://doi.org/10.7302/PTG7-YW20`.

Acknowledgments

The contributions of J.M.B., D.G., and L.G. to this paper were made while they were undergraduate students.

We thank two anonymous reviewers for useful comments that led to improvements in the presentation of this material. We thank Roger Samelson for useful comments on vertical structure and the need to quantify model vertical resolution in the upper ocean, Saulo Muller Soares for pointing us towards the Rimac et al. (2013) reference, Bob Helber for providing climatologies for the vertical mode computations described herein, J. Thomas Farrar, Baylor Fox-Kemper, Jeroen Molemaker, and Joe LaCasce for useful discussions on vertical structure and diurnal variations in the mixed layer, Luca Centurioni and Eric D'Asaro for discussions on the equatorial results, Jonathan M. Lilly for his advice on using jLab, Tong (Tony) Lee for useful discussions on our near-equatorial results, and J. Thomas Farrar for discussions on the potential usefulness of the results shown here for S-MODE and satellite velocity-measuring missions.

B.K.A. gratefully acknowledges funding from US National Science Foundation (NSF) grant OCE-1851164 as well as a Research Experience for Undergraduates Supplement (for J.M.B.) to that grant; from Office of Naval Research (ONR) NISKINE grant N00014-18-1-2544; and from NASA grants NNX16AH79G, NNX17AH55G, and 80NSSC20K1135. The latter NASA grant supported the participation of D.G. and L.G. This research was made possible, in part, by the OSiRIS project at University of Michigan and by computing resources provided by the NASA Advanced Supercomputing (NAS) Division of the Ames Research Center. J.F.S. and M.C.B. acknowledge support by the Office of Naval Research through NISKINE project grants N00014-20-WX01883 (J.F.S.) and N00014-18-1-2801 (M.C.B.). S.E. and E.D.Z. gratefully acknowledges funding from US NSF Awards 1851166 and 1850961, respectively. D.M. carried out research at the Jet Propulsion Laboratory, California Institute of Technology, under contract with NASA, with support from the Physical Oceanography and Modeling, Analysis, and Prediction Programs. A.L.P. and X.Y. are supported by Agence Nationale de la Recherche (ANR) grant number 17-CE01-0006-01. M.H.A. was supported by Office of Naval Research grant N00014-18-1-2404. This NRL contribution NRL/7320/JA–2022/5 has been approved for public release.

This work is a contribution to the S-MODE project, an EVS-3 Investigation awarded under NASA Research Announcement NNH17ZDA001N-EVS3.

References

Alford, M. H. (2003a). Redistribution of energy available for ocean mixing by long-range propagation of internal waves. *Nature*, *423*, 159–162. doi: 10.1038/nature01628

Alford, M. H. (2003b). Improved global maps and 54-year history of wind-work on ocean inertial motions. *Geophysical Research Letters*, *30*, 1424. doi: 10.1029/2002GL016614

Amante, C., & Eakins, B. (2009). Etopo1 1 arc-minute global relief model: Procedures, data sources and analysis. noaa technical memorandum nesdis ngdc-24. national geophysical data center, noaa. (accessed June 28, 2022) doi: 10.7289/V5C8276M

Ansong, J. K., Arbic, B. K., Buijsman, M. C., Richman, J. G., Shriver, J. F., & Wallcraft, A. J. (2015). Indirect evidence for substantial damping of low-mode internal tides in the open ocean. *Journal of Geophysical Research: Oceans*, *120*(9), 6057–6071. doi: 10.1002/2015JC010998

Arbic, B. K. (2022). Incorporating tides and internal gravity waves within global ocean general circulation models: A review. *Progress in Oceanography*. doi: 10.1016/j.pocean.2022.102824

Arbic, B. K., Alford, M., Ansong, J., Buijsman, M., Ciotti, R., Farrar, J., ... Zhao, Z. (2018). A primer on global internal tide and internal gravity wave continuum modeling in HYCOM and MITgcm. In E. Chassignet, A. Pascual, J. Tintoré, & J. Verron (Eds.), *New frontiers in operational oceanography* (pp. 307–392). GODAE Ocean View. doi: 10.17125/gov2018.ch13

Arbic, B. K., Elipot, S., Menemenlis, D., & Shriver, J. F. (2022). *Near-surface oceanic kinetic energy distributions from drifter observations and numerical models [Data set].* University of Michigan–Deep Blue Data. doi: https://doi.org/10.7302/PTG7-YW20

Arbic, B. K., & Flierl, G. R. (2004). Baroclinically unstable geostrophic turbulence in the limits of strong and weak bottom Ekman friction: Application to Midocean Eddies. *Journal of Physical Oceanography*, *34*, 2257-2273. doi: 10.1175/1520-0485(2004)034⟨2257:BUGTIT⟩2.0.CO;2

Arbic, B. K., Richman, J. G., Shriver, J. F., Timko, P. G., Metzger, E. J., & Wallcraf, A. J. (2012). Global modeling of internal tides within an eddying ocean general circulation model. *Oceanography*, *25*, 20–29. doi: 10.5670/oceanog.2012.38

Arbic, B. K., Wallcraft, A. J., & Metzger, E. J. (2010). Concurrent simulation of the eddying general circulation and tides in a global ocean model. *Ocean Modelling*, *32*(3), 175–187. doi: 10.1016/j.ocemod.2010.01.007

Ardhuin, F., Brandt, P., Gaultier, L., Donlon, C., Battaglia, A., Boy, F., ... Stammer, D. (2019). SKIM, a candidate satellite mission exploring global ocean currents and waves. *Frontiers in Marine Science*, *6*, 209. doi: 10.3389/fmars.2019.00209

Aristizábal, M. F., Fewings, M. R., & Washburn, L. (2016). Contrasting spatial patterns in the diurnal and semidiurnal temperature variability in the Santa Barbara Channel, California. *Journal of Geophysical Oceans*, *121*, 427–440. doi: 10.1002/2015JC011239

Beron-Vera, F. J., Olascoaga, M. J., & Miron, P. (2019). Building a maxey–riley framework for surface ocean inertial particle dynamics. *Physics of Fluids*, *31*(9), 096602. doi: 10.1063/1.5110731

Bleck, R. (2002). An oceanic general circulation model framed in hybrid isopycnic-Cartesian coordinates. *Ocean Modelling*, *4*, 55–88. doi: 10.1016/

S1463-5003(01)00012-9

Buijsman, M. C., Ansong, J. K., Arbic, B. K., Richman, J. G., Shriver, J. F., Timko, P. G., ... Zhao, Z. (2016). Impact of parameterized internal wave drag on the semidiurnal energy balance in a global ocean circulation model. *Journal of Physical Oceanography*, *46*, 1399–1419. doi: 10.1175/JPO-D-15-0074.1

Buijsman, M. C., Arbic, B. K., Richman, J. G., Shriver, J. F., Wallcraft, A. J., & Zamudio, L. (2017). Semidiurnal internal tide incoherence in the equatorial Pacific. *Journal of Geophysical Research Oceans*, *122*, 5286–5305. doi: 10.1002/2016JC012590

Buijsman, M. C., Stephenson, G. R., Ansong, J. K., Arbic, B. K., Green, J. A. M., Richman, J. G., ... Zhao, Z. (2020). On the interplay between horizontal resolution and wave drag and their effect on tidal baroclinic mode waves in realistic global ocean simulations. *Ocean Modelling*, *152*, 101656. doi: 10.1016/j.ocemod.2020.101656

Capet, X., McWilliams, J. C., Molemaker, M. J., & Shchepetkin, A. F. (2008). Mesoscale to submesoscale transition in the California Current System. Part III: Energy balance and flux. *Journal of Physical Oceanography*, *38*, 2256–2269. doi: 10.1175/2008JPO3810.1

Chaigneau, A., Pizarro, O., & Rojas, W. (2008). Global climatology of near-inertial current characteristics from Lagrangian observations. *Geophysical Research Letters*, *35*(13), L13603. doi: 10.1029/2008GL034060

Chassignet, E. P., Hurlburt, H. E., Metzger, E. J., Smedstad, O. M., Cummings, J. A., Halliwell, G. R., ... Wilkin, J. (2009). Global ocean prediction with the HYbrid Coordinate Ocean Model (HYCOM). *Oceanography*, *22*. doi: 10.5670/oceanog.2009.39

Chereskin, T. K., Rocha, C., Gille, S. T., Menemenlis, D., & Passaro, M. (2019). Characterizing the transition from balanced to unbalanced motions in the Southern California current. *Journal of Geophysical Research Oceans*, *124*, 2088–2109. doi: 10.1029/2018jc014583

Clayson, C. A., Edson, J. B., Paget, A., Graham, R., & Greenwood, B. (2019). Effects of rainfall on the atmosphere and the ocean during spurs-2. *Oceanography*, *32*, 86–97. doi: 10.5670/oceanog.2019.216

Crawford, G. B., & Large, W. G. (1996). A numerical investigation of resonant inertial response of the ocean to wind forcing. *Journal of Physical Oceanography*, *26*, 873–891. doi: 10.1175/1520-0485(1996)026⟨0873:ANIORI⟩2.0.CO;2

Cronin, M. F., & Coauthors. (2019). Air-sea fluxes with a focus on heat and momentum. *Frontiers in Marine Science*, *6*. doi: 10.3389/fmars.2019.00430

Dohan, K., & Davis, R. E. (2011). Mixing in the transition layer during two storm events. *Journal of Physical Oceanography*, *41*, 42-66. doi: 10.1175/2010JPO4253.1

Egbert, G. D., Bennett, A. F., & Foreman, M. G. G. (1994). TOPEX/POSEIDON tides estimated using a global inverse model. *Journal of Geophysical Research*, *99*, 24821–24852. doi: 10.1029/94JC01894

Egbert, G. D., & Erofeeva, S. Y. (2002). Efficient inverse modeling of barotropic ocean tides. *Journal of Atmospheric and Oceanic Technology*, *19*, 183–204. doi: 10.1175/1520-0426(2002)019⟨0183:EIMOBO⟩2.0.CO;2

Egbert, G. D., & Ray, R. D. (2003). Semi-diurnal and diurnal tidal dissipation from TOPEX/Poseidon altimetry. *Geophysical Research Letters*, *30*, 1907. doi: 10.1029/2003GL017676

Elipot, S. (2006). *Spectral characterization of Ekman velocities in the Southern Ocean based on surface drifter trajectories* (Unpublished doctoral dissertation). Scripps Institution of Oceanography, University of California, San Diego.

Elipot, S. (2020). Measuring global mean sea level changes with surface drifting buoys. *Geophysical Research Letters*, *47*(21), e2020GL091078. doi: 10.1029/2020GL091078

Elipot, S., & Gille, S. T. (2009). Ekman layers in the Southern Ocean: spectral models and observations, vertical viscosity and boundary layer depth. *Ocean Science*, *5*, 115–139. doi: 10.5194/os-5-115-2009

Elipot, S., Lumpkin, R., Perez, R. C., Lilly, J. M., Early, J. J., & Sykulski, A. M. (2016). A global surface drifter data set at hourly resolution. *Journal of Geophysical Research: Oceans*, *121*(5), 2937-2966. doi: 10.1002/2016JC011716

Elipot, S., Lumpkin, R., & Prieto, G. (2010). Modification of inertial oscillations by the mesoscale eddy field. *Journal of Geophysical Research: Oceans*, *115*(C9). doi: 10.1029/2009JC005679

Elipot, S., & Wenegrat, J. O. (2021). Vertical structure of near-surface currents: Importance, state of knowledge, and measurement challenges. *CLIVAR Variations*, *19*. doi: 10.5065/ybca-0s03

Emery, W. J., & Thomson, R. E. (2001). *Data Analysis Methods in Physical Oceanography* (Second and Revised Edition ed.). Elsevier. (638 pp.)

Ferrari, R., & Wunsch, C. (2009). Ocean circulation kinetic energy: Reservoirs, sources and sinks. *Annual Review of Fluid Mechanics*, *41*(1), 253-282. doi: 10.1146/annurev.fluid.40.111406.102139

Flexas, M. M., Thompson, A. F., Torres, H. S., Klein, P. J., Farrar, J. T., Zhang, H., & Menemenlis, D. (2019). Global estimates of the energy transfer from the wind to the ocean, with emphasis on near-inertial oscillations. *Journal of Geophysical Research Oceans*, *124*, 5723–5746. doi: 10.1029/2018JC014453

Furuichi, N., Hibiya, T., & Niwa, Y. (2008). Modelpredicted distribution of windinduced internal wave energy in the world's oceans. *Journal of Geophysical Research*, *113*, C09034. doi: 10.1029/2008JC004768

Garrett, C., & Munk, W. (1975). Space-time scales of internal waves: A progress report. *Journal of Geophysical Research (1896-1977)*, *80*(3), 291–297. doi: 10.1029/JC080i003p00291

Gill, A. E. (1982). *Atmosphere-Ocean Dynamics*. Academic Press.

Gonella, J. (1972). A rotary-component method for analysing meteorological and oceanographic vector time series. *Deep-Sea Research*, *19*, 833–846. doi: 10.1016/0011-7471(72)90002-2

Helber, R. W., Townsend, T. L., Barron, C. N., Dastugue, J. M., & Carnes, M. R. (2013). *Validation test report for the Improved Synthetic Ocean Profile (ISOP) System, Part 1: Synthetic profile methods and algorithm* (Tech. Rep.). NRL Report NRL/MR/7320 13-9364.

Hendershott, M. C. (1972). The effects of solid earth deformation on global ocean tides. *Geophysical Journal International*, *29*, 389–402. doi: 10.1111/j.1365-246X.1972.tb06167.x

Hogan, T. F., Liu, M., Ridout, J. A., Peng, M. S., Whitcomb, T. R., Ruston, B. C., ... Chang, S. W. (2014). The Navy Global Environmental Model. *Oceanography*, *27*, 116–125. doi: 10.5670/oceanog.2014.73

Jayne, S. R., & St. Laurent, L. C. (2001). Parameterizing tidal dissipation over rough topography. *Geophysical Research Letters*, *28*, 811–814. doi: 10.1029/2000GL012044

Kara, A. B., Rochford, P. A., & Hurlburt, H. E. (2000, oct). Efficient and accurate bulk parameterizations of airsea fluxes for use in general circulation models. *Journal of Atmospheric and Oceanic Technology*, *17*(10), 1421–1438. doi: 10.1175/1520-0426(2000)017⟨1421:EAABPO⟩2.0.CO;2

Kerry, C. G., Powell, B. S., & Carter, G. S. (2016). Quantifying the incoherent M_2 internal tide in the Philippine Sea. *Journal of Physical Oceanography*, *46*, 2483–2491. doi: 10.1175/JPO-D-16-0023.1

Kodaira, T., Thompson, K. R., & Bernier, N. B. (2015). Prediction of M_2 tidal surface currents by a global baroclinic ocean model and evaluation using observed drifter trajectories. *Journal of Geophysical Research Oceans*, *121*, 6159–6183. doi: 10.1002/2015JC011549

LaCasce, J. H. (2017). The prevalence of oceanic surface modes. *Geophysical Research Letters*, *44*, 11097–11105. doi: 10.1002/2017GL075430

LaCasce, J. H., & Wang, J. (2015). Estimating subsurface velocities from surface fields with idealized stratification. *Journal of Physical Oceanography*, *45*, 2424-2435. doi: 10.1175/JPO-D-14-0206.1

Lapeyre, G., & Klein, P. (2006). Dynamics of the upper oceanic layers in terms of surface quasigeostrophy theory. *Journal of Physical Oceanography*, *36*, 165–176. doi: 10.1175/JPO2840.1

Large, W. G., & Crawford, G. B. (1995). Observations and simulations of upper-ocean response to wind events during the Ocean Storms Experiment. *Journal of Physical Oceanography*, *25*, 2831–2852. doi: 10.1175/1520-0485(1995)025⟨2831:OASOUO⟩2.0.CO;2

Large, W. G., McWilliams, J. C., & Doney, S. C. (1994). Oceanic vertical mixing: A review and a model with a nonlocal boundary layer parameterization. *Journal of Geophysical Research*, *32*, 363–403. doi: 10.1029/94RG01872

Large, W. G., & Yeager, S. G. (2004). Diurnal to decadal global forcing for ocean and sea-ice models: The data sets and flux climatologies [Tech. Note]. *NCAR Tech. Note*, *TN–460+ST*(May), 105pp. doi: 10.5065/D6KK98Q6

Le Boyer, A., & Alford, M. H. (2021). Variability and sources of the internal wave continuum examined from global moored velocity records. *Journal of Physical Oceanography*, *51*, 2807–2823. doi: 10.1175/JPO-D-20-0155.1

Lévy, M., Franks, P. J., & Smith, K. S. (2018). The role of submesoscale currents in structuring marine ecosystems. *Nature Communications*, *9*. doi: 10.1038/s41467-018-07059-3

Li, Q., Reichl, B. G., FoxKemper, B., Adcroft, A. J., Belcher, S. E., Danabasoglu, G., ... Zheng, Z. (2019). Comparing Ocean Surface Boundary Vertical Mixing Schemes Including Langmuir Turbulence. *Journal of Advances in Modeling Earth Systems*, *11*, 3545–3592. doi: 10.1029/2019MS001810

Lilly, J., & Olhede, S. (2009). Higher-order properties of analytic wavelets. *IEEE Transactions on Signal Processing*, *57*, 146-160. doi: 10.1109/TSP.2008.2007607

Lilly, J. M. (2017). Element analysis : a wavelet-based method for analysing time-localized events in noisy time series Subject Areas : Author for correspondence :. *Proc.R.Soc*(20160776), 473. Retrieved from `http://dx.doi.org/10.1098/rspa.2016.0776`

Lilly, J. M. (2021). *jLab: A data analysis package for Matlab, v.1.7.0 [Data set].* Zenodo. doi: 10.5281/zenodo.4547006

Lilly, J. M. (2022, February). *Ocean/atmosphere time series analysis.* Zenodo. doi: 10.5281/zenodo.5977995

Lilly, J. M., & Elipot, S. (2021). A unifying perspective on transfer function solutions to the unsteady Ekman problem. *Fluids*, *6*(2). Retrieved from `https://www.mdpi.com/2311-5521/6/2/85` doi: 10.3390/fluids6020085

Lilly, J. M., & Olhede, S. C. (2012, nov). Generalized Morse Wavelets as a Superfamily of Analytic Wavelets. *IEEE Trans. Signal Process.*, *60*(11), 6036–6041. Retrieved from `http://ieeexplore.ieee.org/document/6255798/` doi: 10.1109/TSP.2012.2210890

Losch, M., Menemenlis, D., Campin, J.-M., Heimbach, P., & Hill, C. (2010, jan). On the formulation of sea-ice models. Part 1: Effects of different solver implementations and parameterizations. *Ocean Modelling*, *33*(1-2), 129–144. Retrieved from `http://dx.doi.org/10.1016/j.ocemod.2009.12.008https://linkinghub.elsevier.com/retrieve/pii/S1463500309002418` doi: 10.1016/j.ocemod.2009.12.008

Luecke, C. A., Arbic, B. K., Richman, J. G., Shriver, J. F., Alford, M. H., Ansong, J. K., ... Zamudio, L. (2020). Statistical comparisons of temperature variance and kinetic energy in global ocean models and observations: Results

from mesoscale to internal wave frequencies. *Journal of Geophysical Research Oceans*, *125*, e2019JC015306. doi: 10.1029/2019JC015306

Lumpkin, R., & Johnson, G. C. (2013). Global ocean surface velocities from drifters: Mean, variance, El Niño–Southern Oscillation response, and seasonal cycle. *Journal of Geophysical Research: Oceans*, *118*(6), 2992–3006. doi: 10.1002/jgrc.20210

Lumpkin, R., & Pazos, M. (2007). Measuring surface currents with surface velocity program drifters: the instrument, its data and some recent results. *Lagrangian analysis and prediction of coastal and ocean dynamics*, *2*, 39.

Lumpkin, R., zgkmen, T., & Centurioni, L. (2017). Advances in the application of surface drifters. *Annual Review of Marine Science*, *9*(1), 59-81. doi: 10.1146/annurev-marine-010816-060641

Marshall, J., Adcroft, A., Hill, C., Perelman, L., & Heisey, C. (1997). A finite-volume, incompressible Navier Stokes model for studies of the ocean on parallel computers. *Journal of Geophysical Research Oceans*, *102 (C3)*, 5753-5766. doi: 10.1029/96JC02775

Masich, J., Kessler, W. S., Cronin, M. F., & Grissom, K. R. (2021). Diurnal cycles of near-surface currents across the tropical pacific. *Journal of Geophysical Research: Oceans*, *126*, e2020JC016982. doi: 10.1029/2020JC016982

Maximenko, N., Niiler, P., Rio, M.-H., Melnichenko, O., Centurioni, L., Chambers, D., ... Galperin, B. (2009). Mean dynamic topography of the ocean derived from satellite and drifting buoy data using three different techniques. *Journal of Atmospheric and Oceanic Technology*, *26*, 1910–1919. doi: 10.1175/2009JTECHO672.1

Mooers, C. N. (1973). A technique for the cross spectrum analysis of pairs of complex-valued time series, with emphasis on properties of polarized components and rotational invariants. *Deep-Sea Research*, *20*, 1129–1141. doi: 10.1016/0011-7471(73)90027-2

Morrow, R., Fu, L.-L., Ardhuin, F., Benkiran, M., Chapron, B., Cosme, E., ... Zaron, E. D. (2019). Global observations of fine-scale ocean surface topography with the Surface Water and Ocean Topography (SWOT) mission. *Frontiers in Marine Science*, *6*, 232. doi: 10.3389/fmars.2019.00232

Müller, M., Arbic, B. K., Richman, J. G., Shriver, J. F., Kunze, E. L., Scott, R. B., ... Zamudio, L. (2015). Toward an internal gravity wave spectrum in global ocean models. *Geophysical Research Letters*, *42*, 3474–3481. doi: 10.1002/2015GL063365

Müller, M., Cherniawsky, J. Y., Foreman, M. G. G., & von Storch, J.-S. (2012). Global M_2 internal tide and its seasonal variability from high resolution ocean circulation and tide modeling. *Geophysical Research Letters*, *39*(19). doi: 10.1029/2012GL053320

Nelson, A. D., Arbic, B. K., Mememenlis, D., Peltier, W. R., Grisouard, N., & Klymak, J. M. (2020). Improved internal wave spectral continuum in a regional ocean model. *Journal of Geophysical Research Oceans*, *125*, e2019JC015974. doi: 10.1029/2019JC015974

Nelson, A. D., Arbic, B. K., Zaron, E. D., Savage, A. C., Richman, J. G., & Buijsman, J. F., M. C. Shriver. (2019). Toward realistic nonstationarity of semidiurnal baroclinic tides in a hydrodynamic model. *Journal of Geophysical Research Oceans*, *124*, 6632–6642. doi: 10.1029/2018JC014737

Ngodock, H. E., Souopgui, I., Wallcraft, A. J., Richman, J. G., Shriver, ., Jay F., & Arbic, B. K. (2016). On improving the accuracy of the M_2 barotropic tides embedded in a high-resolution global ocean circulation model. *Ocean Modelling*, *97*, 16–26. doi: 10.1016/j.ocemod.2015.10.011

Niiler, P. P., & Paduan, J. D. (1995). Wind-driven motions in the Northeast Pacific as measured by Lagrangian drifters. *Journal of Physical Oceanography*, *25*(11), 2819–2830. doi: 10.1175/1520-0485(1995)025⟨2819:WDMITN⟩2.0.CO;2

Pan, Y., Arbic, B. K., Nelson, A. D., Menemenlis, D., Peltier, W. R., Xu, W., & Li, Y. (2020). Numerical investigation of mechanisms underlying oceanic internal gravity wave power-law spectra. *Journal of Physical Oceanography*, *50*. doi: 10.1175/JPO-D-20-0039.1

Pollard, R. T., & Millard, R. C. (1970). Comparison between observed and simulated wind-generated inertial oscillations. *Deep-Sea Research*, *17*, 813–821. doi: 10.1016/0011-7471(70)90043-4

Polton, J. A., Lewis, D. M., & Belcher, S. E. (2005). The role of wave-induced Coriolis–Stokes forcing on the wind-driven mixed layer. *Journal of Physical Oceanography*, *35*(4), 444–457. doi: https://doi.org/10.1175/JPO2701.1

Ponte, A. L., & Klein, P. (2015). Incoherent signature of internal tides on sea level in idealized numerical simulations. *Geophysical Research Letters*, *42*, 1520–1526. doi: 10.1002/2014GL062583

Pottapinjara, V., & Joseph, S. (2022). Evaluation of mixing schemes in the HYbrid Coordinate Ocean Model (HYCOM) in the tropical Indian Ocean. *Ocean Dynamics*, *72*, 341–359. doi: 10.1007/s10236-022-01510-2

Poulain, P.-M., & Centurioni, L. (2015). Direct measurements of World Ocean tidal currents with surface drifters. *Journal of Geophysical Research: Oceans*, *120*(10), 6986–7003. doi: 10.1002/2015JC010818

Price, J. F., & Sundermeyer, M. A. (1999). Stratified Ekman layers. *Journal of Geophysical Research*, *104*, 20467–20494. doi: 10.1029/1999JC900164

Price, J. F., Weller, W. A., & Pinkel, R. (1986). Diurnal cycling: Observations and models of the upper ocean response to diurnal heating, cooling and wind mixing. *Journal of Geophysical Research*, *91*, 8411–8427. doi: 10.1029/JC091iC07p08411

Qiu, B., Chen, S., Klein, P., Wang, J., Torres, H., & Fu, L.-L. (2018). Seasonality in transition scale from balanced to unbalanced motions in the world ocean. *Journal of Physical Oceanography*, *48*, 591–605. doi: 10.1175/JPO-D-17-0169.1

Ray, R. D. (1998). Ocean self-attraction and loading in numerical tidal models. *Marine Geodesy*, *21*, 181–192. doi: 10.1080/01490419809388134

Ray, R. D., & Zaron, E. D. (2011). Nonstationary internal tides observed with satellite altimetry. *Geophysical Research Letters*, *38*, L17609. doi: 10.1029/2011GL048617

Richman, J. G., Arbic, B. K., Shriver, J. F., Metzger, E. J., & Wallcraft, A. J. (2012). Inferring dynamics from the wavenumber spectra of an eddying global ocean model with embedded tides. *Journal of Geophysical Research: Oceans*, *117*(C12). doi: 10.1029/2012JC008364

Rimac, A., von Storch, J.-S., Eden, C., & Haak, H. (2013). The influence of high-resolution wind stress field on the power input to near-inertial motions in the ocean. *Geophysical Research Letters*, *40*, 4882–4886. doi: 10.1002/grl.50929

Rocha, C. B., Chereskin, T. K., Gille, S. T., & Menemenlis, D. (2016). Mesoscale to submesoscale wavenumber spectra in Drake Passage. *Journal of Physical Oceanography*, *46*(2), 601–620. doi: 10.1175/JPO-D-15-0087.1

Rocha, C. B., Gille, S. T., Chereskin, T. K., & Menemenlis, D. (2016). Seasonality of submesoscale dynamics in the Kuroshio Extension. *Geophysical Research Letters*, *43*(21), 11,304–311,311. doi: 10.1002/2016GL071349

Rodriguez, E., Wineteer, A., Perkovic-Martin, D., Gal, T., Anderson, S., Zuckerman, S., ... Yang, X. (2020). Ka-Band Doppler scatterometry over a Loop Current eddy. *Remote Sensing*, *12*, 2388. doi: 10.3390/rs12152388

Samelson, R. M. (2022). Wind drift in a homogeneous equilibrium sea. *Journal of Physical Oceanography*, *52*, 1945–1967. doi: 10.1175/JPO-D-22-0017.1

Savage, A. C., Arbic, B. K., Alford, M. H., Ansong, J. K., Farrar, J. T., Menemenlis, D., ... Zamudio, L. (2017b). Spectral decomposition of internal gravity wave sea surface height in global models. *Journal of Geophysical Research: Oceans*,

122(10), 7803–7821. doi: 10.1002/2017JC013009

Savage, A. C., Arbic, B. K., Richman, J. G., Shriver, J. F., Alford, M. H., Buijsman, M. C., ... Zamudio, L. (2017a). Frequency content of sea surface height variability from internal gravity waves to mesoscale eddies. *Journal of Geophysical Research: Oceans*, *122*(3), 2519–2538. doi: 10.1002/2016JC012331

Shriver, J. F., Richman, J. G., & Arbic, B. K. (2014). How stationary are the internal tides in a high-resolution global ocean circulation model? *Journal of Geophysical Research Oceans*, *119*, 2769–2787. doi: 10.1002/2013JC009423

Simmons, H. L., & Alford, M. H. (2012). Simulating the long-range swell of internal waves generated by ocean storms. *Oceanography*, *25*, 30–41. doi: 10.5670/oceanog.2012.39

Sun, D., Bracco, A., Barkan, R., Berta, M., Dauhajre, D., Molemaker, M. J., ... McWilliams, J. C. (2020). Diurnal cycling of submesoscale dynamics: Lagrangian implications in drifter observations and model simulations of the Northern Gulf of Mexico. *Journal of Physical Oceanography*, *50*, 1605–1623. doi: 10.1175/JPO-D-19-0241.1

Sun, W.-Y., & Sun, O. M. (2020). Inertia and diurnal oscillations of Ekman layers in atmosphere and ocean. *Dynamics of Atmospheres and Oceans*, *90*, 101144. doi: 10.1016/j.dynatmoce.2020.101144

Sutherland, G., Marié, L., Reverdin, G., Christensen, K. H., Broström, G., & Ward, B. (2016). Enhanced turbulence associated with the diurnal jet in the ocean surface boundary layer. *Journal of Physical Oceanography*, *46*, 3051–3067. doi: 10.1175/JPO-D-15-0172.1

Thompson, E. J., Asher, W. E., Jessup, A. T., & Drushka, K. (2019). High-resolution rain maps from an x-band marine radar and their use in understanding ocean freshening. *Oceanography*, *32*, 58–65. doi: 10.5670/oceanog.2019.213

Thoppil, P. G., Richman, J. G., & Hogan, P. J. (2011). Energetics of a global ocean circulation model compared to observations. *Geophysical Research Letters*, *38*(15). doi: 10.1029/2011GL048347

Thyng, K. M., Greene, C. A., Hetland, R. D., Zimmerle, H. M., & DiMarco, S. F. (2016). True colors of oceanography: Guidelines for effective and accurate colormap selection. *Oceanography*, *29*, 9–13. doi: 10.5670/oceanog.2016.66

Timko, P. G., Arbic, B. K., Richman, J. G., Scott, R. B., Metzger, E. J., & Wallcraft, A. J. (2013). Skill testing a three-dimensional global tide model to historical current meter records. *Journal of Geophysical Research Oceans*, *118*, 6914–6933. doi: 10.1002/2013JC009071

Torres, H. S., Klein, P., Menemenlis, D., Qiu, B., Su, Z., Wang, J., ... Fu, L.-L. (2018). Partitioning ocean motions into balanced motions and internal gravity waves: A modeling study in anticipation of future space missions. *Journal of Geophysical Research: Oceans*, *123*(11), 8084–8105. doi: 10.1029/2018JC014438

Trossman, D. S., Arbic, B. K., Straub, D. N., G, R. J., Chassignet, E. P., Wallcraft, A. J., & Xu, X. (2017). The role of rough topography in mediating impacts of bottom drag in eddying ocean circulation models. *Journal of Physical Oceanography*, *47*, 1941-1959. doi: 10.1175/JPO-D-16-0229.1

Van Roekel, L., Adcroft, A. J., Danabasoglu, G., Griffies, S. M., Kauffman, B., Large, W., ... Schmidt, M. (2018). The KPP boundary layer scheme for the ccean: Revisiting its formulation and benchmarking onedimensional simulations relative to LES. *Journal of Advances in Modeling Earth Systems*, *10*, 2647–2685. doi: 10.1029/2018MS001336

Wang, J., Fu, L.-L., Qiu, B., Menenemlis, D., Farrar, J. T., Chao, Y., ... Flexas, M. M. (2018). An observing system simulation experiment for the calibration and validation of the Surface Water Ocean Topography sea surface height measurement using in situ platforms. *Journal of Atmospheric and Oceanic*

Technology, *35*. doi: 10.1175/JTECH-D-17-0076.1

Wang, Y., Xu, Z., Hibiya, T., Yin, B., & Wang, F. (2021). Radiation path of diurnal internal tides in the Northwestern Pacific controlled by refraction and interference. *Journal of Geophysical Research: Oceans*, *126*, e2020JC016972. doi: 10.1029/2020JC016972

Waterhouse, A. F., MacKinnon, J. A., Nash, J. D., Alford, M. H., Kunze, E., Simmons, H. L., ... Lee, C. M. (2014). Global Patterns of Diapycnal Mixing from Measurements of the Turbulent Dissipation Rate. *Journal of Physical Oceanography*, *44*(7), 1854–1872. doi: 10.1175/JPO-D-13-0104.1

Wunsch, C. (1997). The vertical partition of oceanic horizontal kinetic energy. *Journal of Physical Oceanography*, *27*, 1770–1794. doi: 10.1175/1520-0485(1997)027⟨1770:TVPOOH⟩2.0.CO;2

Yu, X., Ponte, A. L., Elipot, S., Menemenlis, D., Zaron, E. D., & Abernathey, R. (2019). Surface kinetic energy distributions in the global oceans from a high-resolution numerical model and surface drifter observations. *Geophysical Research Letters*, *46*(16), 9757–9766. doi: 10.1029/2019GL083074

Zaron, E. D. (2017). Mapping the nonstationary internal tide with satellite altimetry. *Journal of Geophysical Research Oceans*, *122*, 539–554. doi: 10.1002/2016JC012487

Zaron, E. D., & Egbert, G. D. (2014). Time-variable refraction of the internal tide at the Hawaiian Ridge. *Journal of Physical Oceanography*, *44*, 538–557. doi: 10.1175/JPO-D-12-0238.1

Zaron, E. D., & Elipot, S. (2021). An assessment of global ocean barotropic tide models using geodetic mission altimetry and surface drifters. *Journal of Physical Oceanography*, *51*, 63-82. doi: 10.1175/JPO-D-20-0089.1